Numerical Simulation of Tornadogenesis in a High-Precipitation Supercell. Part I: Storm Evolution and Transition into a Bow Echo

Catherine A. Finley,* W. R. Cotton, and R. A. Pielke Sr.

Department of Atmospheric Science, Colorado State University, Fort Collins, Colorado

ABSTRACT

A nested grid primitive equation model (RAMS version 3b) was used to simulate a high-precipitation (HP) supercell, which produced two weak tornadoes. Six telescoping nested grids allowed atmospheric flows ranging from the synoptic scale down to the tornadic scale to be represented in the simulation. All convection in the simulation was initiated with resolved vertical motion and subsequent condensation–latent heating from the model microphysics; no warm bubbles or cumulus parameterizations were used.

Part I of this study focuses on the simulated storm evolution and its transition into a bow echo. The simulation initially produced a classic supercell that developed at the intersection between a stationary front and an outflow boundary. As the simulation progressed, additional storms developed and interacted with the main storm to produce a single supercell. This storm had many characteristics of an HP supercell and eventually evolved into a bow echo with a rotating comma-head structure. An analysis of the storm's transition into a bow echo revealed that the interaction between convective cells triggered a series of events that played a crucial role in the transition.

The simulated storm structure and evolution differed significantly from that of classic supercells produced by idealized simulations. Several vertical vorticity and condensate maxima along the flanking line moved northward and merged into the mesocyclone at the northern end of the convective line during the bow echo transition. Vorticity budget calculations in the mesocyclone showed that vorticity advection from the flanking line into the mesocyclone was the largest positive vorticity tendency term just prior to and during the early phase of the transition in both the low- and midlevel mesocyclone, and remained a significant positive tendency in the midlevel mesocyclone throughout the bow echo transition. This indicates that the flanking line was a source of vertical vorticity for the mesocyclone, and may explain how the mesocyclone was maintained in the HP supercell even though it was completely embedded in heavy precipitation.

The simulated supercell also produced two weak tornadoes. The evolution of the simulated tornadoes and an analysis of the tornadogenesis process will be presented in Part II.

1. Introduction

The term supercell was first used by Browning (1964, 1968) in reference to storms that exhibited evidence of strong rotation when viewed with time-lapse photography. In recent years, supercells have been generally defined as storms with significant persistent spatial correlations between updraft centers and vorticity centers (Weisman and Klemp 1984; Doswell and Burgess 1993). Supercells generally fall into three different categories depending on their precipitation structure and characteristics (Bluestein and Parks 1983; Moller and Doswell 1988; Doswell et al. 1990; Doswell and Burgess 1993; Moller et al. 1994): low-precipitation (LP) supercells, "classic" supercells, and high-precipitation (HP) supercells.

Classic supercells are perhaps the most studied of the supercell spectrum. The conceptual model of a classic supercell was first introduced by Browning (1964) and has changed little in the last 20 years. Most of the precipitation falls downwind from the main storm updraft, which lies above the intersection of the forward flank and rear flank gust fronts. Tornadoes usually develop in regions where the environmental inflow and storm outflow meet beneath the mesocyclone or along the nose of the gust front.

High-precipitation supercells occur most frequently in the eastern half of the United States and western high plains (Doswell and Burgess 1993) and may be the predominant type of supercell in these regions. Foote and Frank (1983), Doswell (1985), Vasiloff et al. (1986), Nelson (1987), Nelson and Knight (1987), Moller and Doswell (1988), Przybylinski (1989), Doswell et al. (1990), Moller et al. (1990), Przybylinski et al. (1990), Doswell and Burgess (1993), Imy and Pence (1993),

* Current affiliation: Department of Earth Sciences, University of Northern Colorado, Greeley, Colorado.

Corresponding author address: Dr. Catherine Finley, Department of Earth Sciences, University of Northern Colorado, Greeley, CO 80639.
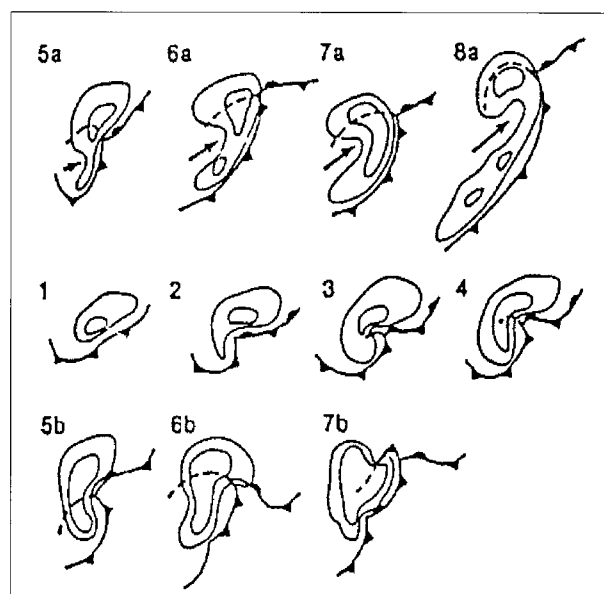E-mail: cafinle@bentley.unco.edu

FIG. 1. Possible life cycles (as seen on radar) of HP supercells. Frames 1–4 indicate the transition of a classical supercell into an HP supercell. The HP supercells may then evolve into a bow echo with a rotating comma head (5a–8a) or may produce cyclic mesocyclones along the storms' southern flank (5b–7b) in a manner similar to classical supercells. Arrows denote the location of the rear inflow jet in 5a–8a (from Moller et al. 1990).

Przybylinski et al. (1993), Moller et al. (1994), and Calianese et al. (1996) have documented the following characteristics of HP supercells.

- HP storms often develop and move along a preexisting thermal boundary, usually an old outflow boundary or stationary front.
- HP storms tend to be larger than classic supercells.
- Extensive precipitation occurs along the right-rear flank of storm.
- The mesocyclone is frequently embedded in significant precipitation and is often located on the right forward flank of the storm.
- HP storms are often associated with widespread damaging hail or wind events, with damage occurring over relatively long and broad swaths. It has been suggested that derechos may have HP supercells embedded in them (Johns and Hirt 1987).
- Radar signatures of HP supercells include kidney-bean, spiral, comma-head or S-shaped structures, and exceptionally large hook echoes.
- HP supercells may exhibit multicell characteristics such as several high reflectivity cores, multiple mesocyclones, and multiple bounded weak echo regions.
- Tornadoes may occur with the mesocyclone or along the leading edge of the gust front. If the storm evolves into a bow echo, tornadoes sometimes develop in the rotating comma-head portion of the storm.

High-precipitation supercells can also follow several different life cycles as shown in Fig. 1. Frames 1–4

show the transition of a classic supercell into an HP supercell. Note that the mesocyclone is located on the forward flank of the HP supercell, not along the right-rear flank as with classic supercells. The storm can then evolve into a bow echo storm with a rotating comma-head structure (an evolution that usually occurs in a rapid transition) or develop a new mesocyclone along the right-rear flank as the old mesocyclone moves along the leading edge of the storm and dissipates. Cyclic mesocyclone development has been observed to occur with either life cycle (Moller et al. 1990) as patterns 2–8a or 2–7b are repeated during the storm evolution. Little is known as to how or why some HP storms transition into bow echoes, although Moller et al. (1994) state that "those HP storms that *do* develop bow echo structures are not as isolated from surrounding convection as LP or classic storms, although they remain 'distinctive' in character."

Previous studies of classic supercells have shown that midlevel rotation originates from tilting of environmental low-level streamwise vorticity by the updraft (Klemp and Wilhelmson 1978a,b; Klemp et al. 1981; Rotunno 1981; Weisman and Klemp 1982, 1984; Davies-Jones 1984), and low-level storm rotation originates from tilting of baroclinically generated horizontal vorticity created along the forward flank gust front (Klemp and Rotunno 1983; Rotunno and Klemp 1985; Davies-Jones and Brooks 1993; Wicker and Wilhelmson 1995). However, HP supercells may exhibit flow characteristics slightly different from their classic cousins. Lemon (1976) used radar observations to document an HP supercell where cells in the flanking line merged with the mesocyclone. During the merger, the updraft velocity increased, the surface pressure beneath the mesocyclone dropped, the rotation increased. Barnes (1978a) also observed a storm in which mesocyclone rotation may have increased following merger with a rotating updraft that originated along the flanking line. Recently, Kulie and Lin (1998) performed a model simulation of a hybrid multicell–supercell storm. In their simulation, the main storm updraft and mesocyclone reintensified following the merger between a cell along the flanking line and the main updraft. They speculated that these mergers may play an important role in maintaining storm-scale rotation and updraft intensity.

Until recently, most numerical simulations of severe storms have started with horizontally homogeneous initial conditions in which a single "typical" sounding is used to initialize the entire model domain (Klemp and Wilhelmson 1978a,b; Klemp et al. 1981; Weisman and Klemp 1982, 1984; Droegemeier et al. 1993). Since there are no inhomogeneities to drive convergence in these simulations, covective storms are initiated by a warm bubble. These numerical studies have been able to simulate many aspects of classic supercell storms, but there have been only a few such modeling studies of other types of supercell storms (Brooks and Wilhelmson 1992; Kulie and Lin 1998).
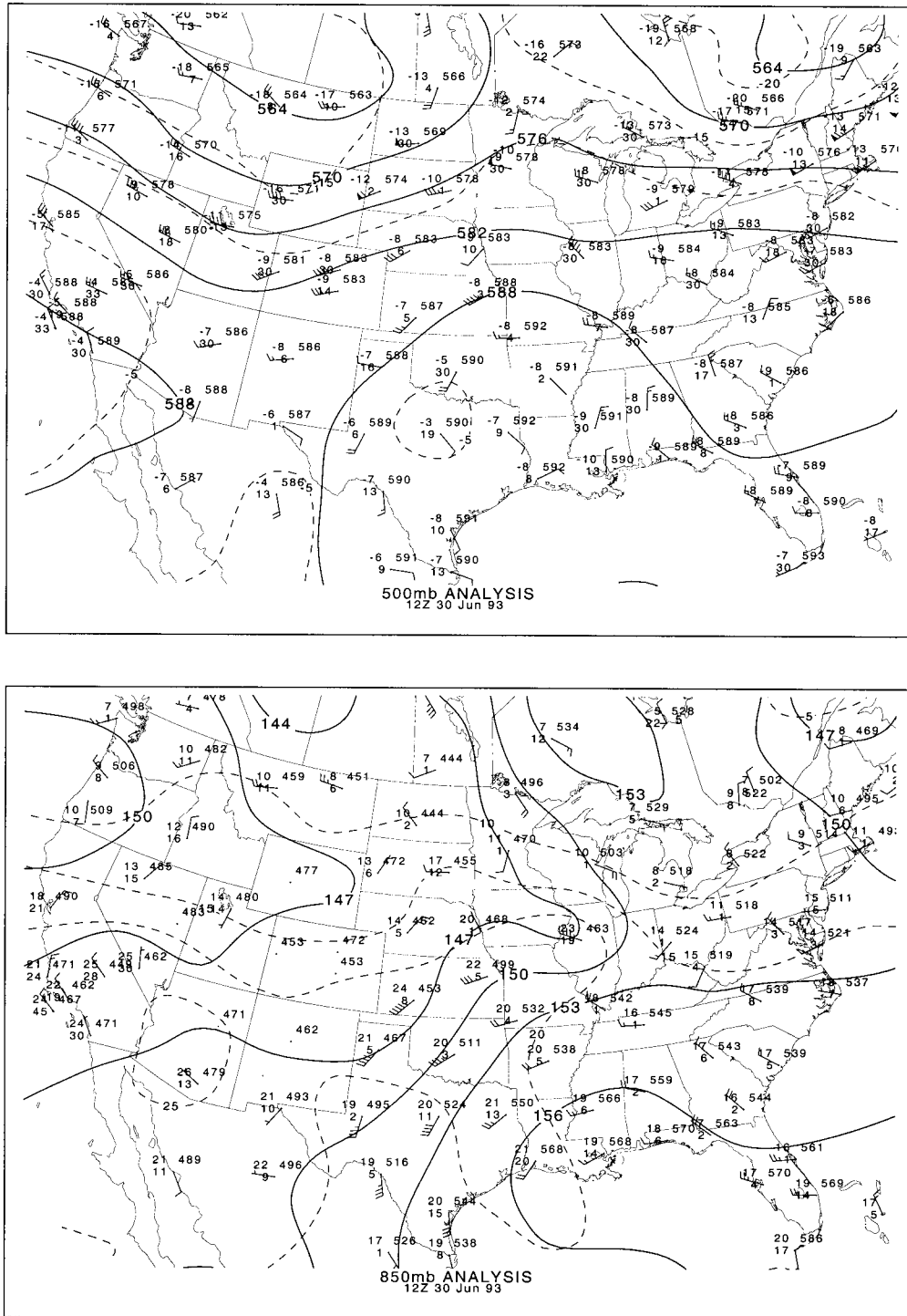
FIG. 2. (top) The 500-mb analysis and (bottom) the 850-mb analysis at 1200 UTC 30 Jun 1993.

The fact that convective characteristics and evolution may be sensitive to the initial forcing in simulations using horizontally homogeneous initial conditions has been demonstrated in several numerical studies. Brooks and Wilhelmson (1992) were able to simulate a storm that had many features of observed LP storms using horizontally homogeneous initial conditions. The LP storm was produced in an environment normally associated with classic supercells (and in one of their simulations, this sounding did produce a classic supercell), but a smaller temperature perturbation was used to initiate convection. McPherson and Droegemeier (1991)

also found that storm evolution beyond 75 min in their simulations was sensitive to the size and strength of the initial convective bubble. This is disconcerting from a modeling standpoint since it shows that even the *qualitative* model results may be sensitive to the way convection is initiated. Using horizontally homogeneous initial conditions may also present other limitations in severe storms modeling. Doswell et al. (1990) state that ''the mesoscale variations necessitating inhomogeneous initial conditions may well have been an important factor in the convective evolution.'' They also point out that it is not necessarily true that *all* forms of supercell behavior can be simulated well with horizontally homogeneous initial conditions.

In this study, a nested grid primitive equation model (RAMS version 3b), which was initialized with synoptic data from 30 June 1993 is used to study the transition of an HP supercell into a bow echo. The use of synoptic data provides the inhomogeneities necessary to initiate convection, and the use of telescoping nested grids allows the simulated environment to trigger convection explicitly without the use of warm bubbles or cumulus parameterization. Similar approaches were used by Grasso (1996), Bernardet and Cotton (1998), and Nachamkin and Cotton (2000) to simulate convection. Although the model initial conditions were derived from synoptic data, they are still an approximation to reality. Thus, it is difficult to say that one is simulating the *exact* observed storm at a given time and location. However, simulations of this type should be able to produce storms that are representative of the type of convection that occurred on a given day, and reproduce some aspects of storm behavior not captured in horizontally homogeneous simulations.

In the simulation presented here, a total of six grids were used. Grids 1–2 captured the evolution of the synoptic-scale features while grid 3 captured the mesoscale features in the storm environment. Grids 4–5 were used to resolve the supercell storms that developed, and grid 6 captured the evolution of the tornadoes. A unique aspect of this simulation is that atmospheric flows ranging from the synoptic scale down to the tornado scale can be simultaneously represented. The focus of this paper is the development and evolution of a simulated HP supercell and its transition into a comma-shaped bow echo. The synoptic conditions and the observations of convection on 30 June 1993 are presented in section 2. The model used in this study is described in section 3, and the storm evolution in the simulation is presented in section 4. An analysis of the storm's transition into a bow echo structure is given in section 5, and a summary and discussion of the results is contained in section 6. The simulated storm produced two tornado-like vortices which will be the focus of Part II of this study.

2. 30 June 1993 case overview

At upper levels at 1200 UTC 30 June, weak southwesterly flow was evident across Nebraska, Kansas, and Missouri with a weak shortwave embedded in the flow over the Great Basin/Central Rockies. The flow was diffluent from 500 to 200 mb (Fig. 2) over Iowa, Missouri, and eastern parts of Nebraska and Kansas from 1200 UTC 30 June at least through 0000 UTC 1 July. A 30–40 kt low-level jet between 925 and 850 mb was bringing gulf moisture northward into the central plains, with 850-mb dewpoints ranging from 15° to 20°C, supporting almost continuous convection over the Midwest.

The surface synoptic situation on the morning of the 30th was quite complex. The previous evening, a Mesoscale Convective Complex (MCC) produced heavy rains over Iowa. By 1200 UTC 30 June, the system had moved into Illinois and Indiana. New convective cells formed to the west of the system during the early morning hours of 30 June, so that by sunrise, rain was again falling over much of the eastern half of Nebraska and northeast Kansas. A stationary front stretched from southeast Colorado to a weak area of low pressure in southwest Iowa. Another quasi-stationary front extended from the low in Iowa to another weak low in western Indiana. These surface features remained quasi-stationary during the day and into the nighttime hours. South of the frontal boundaries, dewpoints ranged from 21°–26°C while north of the front, dewpoints ranged from 14°–18°C. The morning convection in Iowa produced an outflow boundary that moved southward and then stalled across northern Missouri and northeast Kansas by 2000 UTC as shown in Fig. 3. This outflow boundary remained stationary through the afternoon hours, and played an instrumental role in initiating convection.

The storm of interest in this study began to develop between 2100 and 2130 UTC at the intersection between the stationary front and the outflow boundary in northeast Kansas. In the next hour, the storm evolved into a supercell (Fig. 4) and severe weather began to be reported around 2330 UTC. By 0100 UTC 1 July, this storm became part of a squall line that extended from northeast Kansas into central Iowa, and eventually developed into an MCC.

During the early part of its life, the storm moved slowly eastward producing 8–13 cm of rain in 2 h in parts of northeast Kansas, large hail and winds 27–32 m s^{-1} in some locations. The storm system also produced six confirmed weak (F0–F1) tornadoes in northeast Kansas, with many more reports of funnel clouds from the general public.

3. Model description and configuration

The Regional Atmospheric Modeling System (RAMS) version 3b developed at Colorado State University was used for the simulation. Important aspects of the model are briefly overviewed here. A more complete discussion can be found in Pielke et al. (1992) and Finley (1998). The model utilizes a staggered Arakawa C grid (Arakawa and Lamb 1981) with terrain-following sigma coordinates in the vertical (Tripoli and Cotton
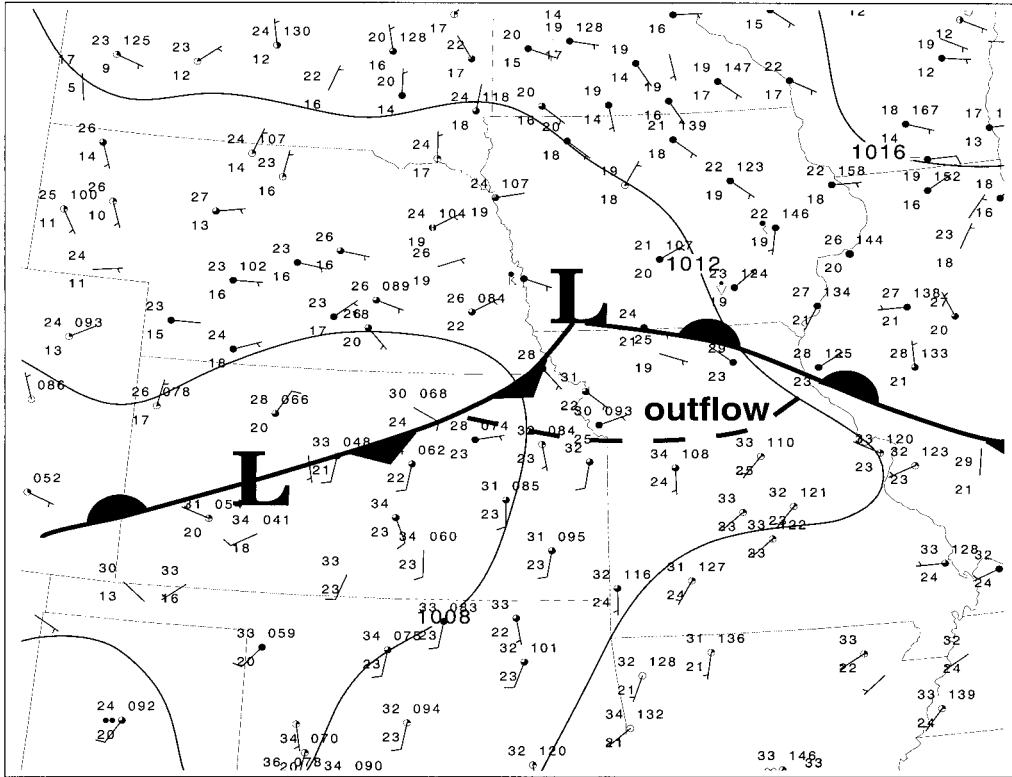
FIG. 3. Surface analysis at 2000 UTC 30 Jun 1993. Note the outflow boundary that has moved into northern Missouri and northeast Kansas.

1980). A second-order hybrid time step scheme was used in which momentum fields were advanced using a leapfrog scheme, and scaler fields were advanced using a forward scheme. The nonhydrostatic compressible forms of the basic model equations (Tripoli and Cotton 1986) were used and subgrid-scale turbulence was parameterized following Smagorinsky (1963) with stability modifications by Lilly (1962) and Hill (1974).

FIG. 4. Radar summary at 2235 UTC 30 Jun 1993. The storm of interest is the supercell developing in northeast Kansas.

The radiation scheme used was developed by Maher and Pielke (1977). Radiative fluxes are calculated as functions of the vertical temperature and moisture distributions, and incoming solar radiation varies longitudinally to account for the diurnal cycle. Clouds are seen only as areas of very high water vapor content, and the radiative characteristics of condensed liquid and ice species are not accounted for. This leads to an overestimate of solar fluxes reaching the surface in cloudy regions and an underestimate of the longwave cooling at the top of clouds. These errors most likely did not have a large impact on the simulation since supercell thunderstorms are largely dynamically (not radiatively) driven systems. However, a recent observational study by Markowski et al. (1998) suggested that baroclinic zones generated by anvil shadows along the storm's forward flank could enhance storm rotation. Their study found that parcels traveling through this baroclinic zone en route to the updraft could acquire significant horizontal vorticity. This potential effect is not included in the present simulation.

Condensed water species are represented with a single-moment bulk microphysics parameterization (Walko et al. 1995). This includes predictive equations for the mixing ratios of rain, snow, aggregates, graupel and hail, as well as the concentration of pristine ice. Cloud water is diagnosed as a residual. No cumulus parameterization
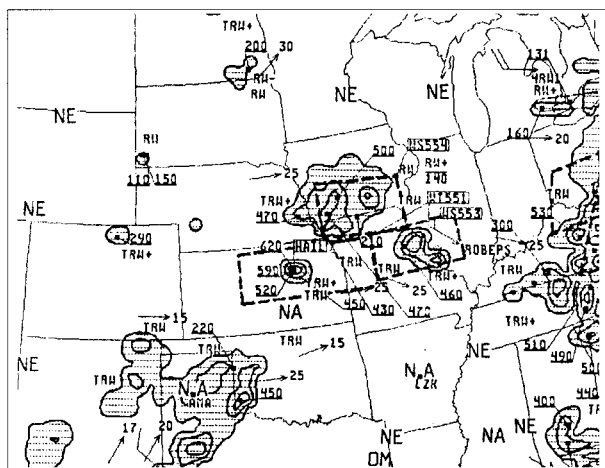
was used in the simulation. All convection was generated by resolved vertical motions and subsequent condensation–latent heating.

RAMS also possesses a soil model (Tremback and Kessler 1985) and a vegetation parameterization (Avissar and Pielke 1989). The soil model is a multilayer column model in which heat and moisture are exchanged vertically between soil layers and the atmosphere. Vegetation was classified into 18 different categories, each category with its own value for leaf area index, roughness length, displacement height, and root parameters.

Two-way interactive grid nesting (Clark and Farley 1984) was used to reduce memory and computational requirements by increasing horizontal resolution only over the region(s) of interest. Grids 4–6 were also moved within their respective parent grids (Walko et al. 1995), further reducing the number of grid points needed since the phenomenon of interest cloud be "followed."

The model initial conditions and the time-dependent lateral boundary conditions were derived from a Barnes objective analysis (Barnes 1964, 1973) of several datasets available at the National Center for Atmospheric Research (NCAR). These datasets include the NCEP spectral model analyses, upper-air observations, hourly surface observations, and hourly wind profiler data. The initialization captured the basic synoptic-scale features such as the low in southeast Colorado, the stationary front across Kansas and Nebraska, and remnants of an old storm outflow across Missouri and Illinois. Both the lateral and top boundary conditions for grid 1 were provided with a Davies nudging scheme (Davies 1976). An interior nudging option was also used early in the simulation to incorporate an important outflow boundary that was not present at the time the model was initialized. This procedure will be discussed in more detail in section 4.

Topography on grid 1 was generated using the U.S. Geological Survey (USGS) 10 minute dataset, while on grid 2, the USGS 30 second dataset was used. Sea surface temperatures (SSTs) were provided by the 1° monthly mean values as given in the NCAR SST dataset. Vegetation type and land percentage were provided by the USGS 30 second land use dataset (Loveland et al. 1991). The original vegetation dataset contains 159 different land use categories (including water), which are converted to 18 categories used by the model, based on the dominant vegetation type in each grid cell.

Since no consolidated national soil moisture databases exist, soil moisture was initialized using an Antecedent Precipitation Index (API) (Wetzel and Chang 1988). This procedure utilizes the previous 3 months of precipitation in which observations closer to the model start time are weighted more heavily. In this particular case, the API underestimated soil moisture in the Midwest since the regression is based on a "normal" year of precipitation. Soil type is assumed constant throughout the model domain in the absence of any easily accessible soil databases.

TABLE 1. Summary of the grid configuration used in the simulation.

	30 Jun case
Grid 1	Grid spacing: 120 km 44 × 34 points Time step: 90 s
Grid 2	Grid spacing: 40 km 44 × 50 points Time step: 45 s
Grid 3	Grid spacing: 8 km 42 × 42 points Time step: 15 s
Grid 4	Grid spacing: 1.6 km 57 × 57 Time step: 5 s
Grid 5	Grid spacing: 400 m 90 × 90 points Time step: 2.5 s
Grid 6	Grid spacing: 100 m 62 × 62 points Time step: 0.83 s
Vertical grid spacing	Starts at 80 m—stretched to 1 km at upper levels
Soil layers	7 points at depths of 0 cm (surface), 3 cm, 6 cm, 9 cm, 18 cm, 35 cm, 50 cm

One of the largest obstacles to modeling tornadic supercells starting with synoptic data is the great range of spatial scales that need to be resolved. This makes such simulations computationally expensive. In the simulation presented here, six grids were required to capture the full range of scales (Table 1). The geographical location of each grid is shown in Fig. 5. Since grids 4–6 were moved during the simulation, they are shown in their initial positions with respect to their parent grids.

The simulation was started at 1200 UTC 30 June 1993 and ended at 0100 UTC 1 July. The simulation began with grids 1–3 from 1200 to 2000 UTC to capture the early evolution of the synoptic fields. Grid 4 was added at 2000 UTC at which point the microphysics parameterization was activated. Grid 4 captured the development and evolution of the thunderstorm complex until 0000 UTC 1 July at which point grids 5–6 were added. All six grids were then run until the end of the simulation at 0100 UTC.

4. Simulated storm evolution and structure

The morning convection over Nebraska and Iowa was not captured in the simulation, despite attempts with a cumulus parameterization and different grid configurations. Hence the outflow boundary produced by this convection never developed in the simulation. Simulations performed without the outflow boundary in the model fields failed to produce convection in northeast Kansas, although they did capture the convection that later developed in southwestern Iowa. Stensrud and Fritsch (1994a,b) illustrated the importance of incorporating mesoscale features into simulations of convec-
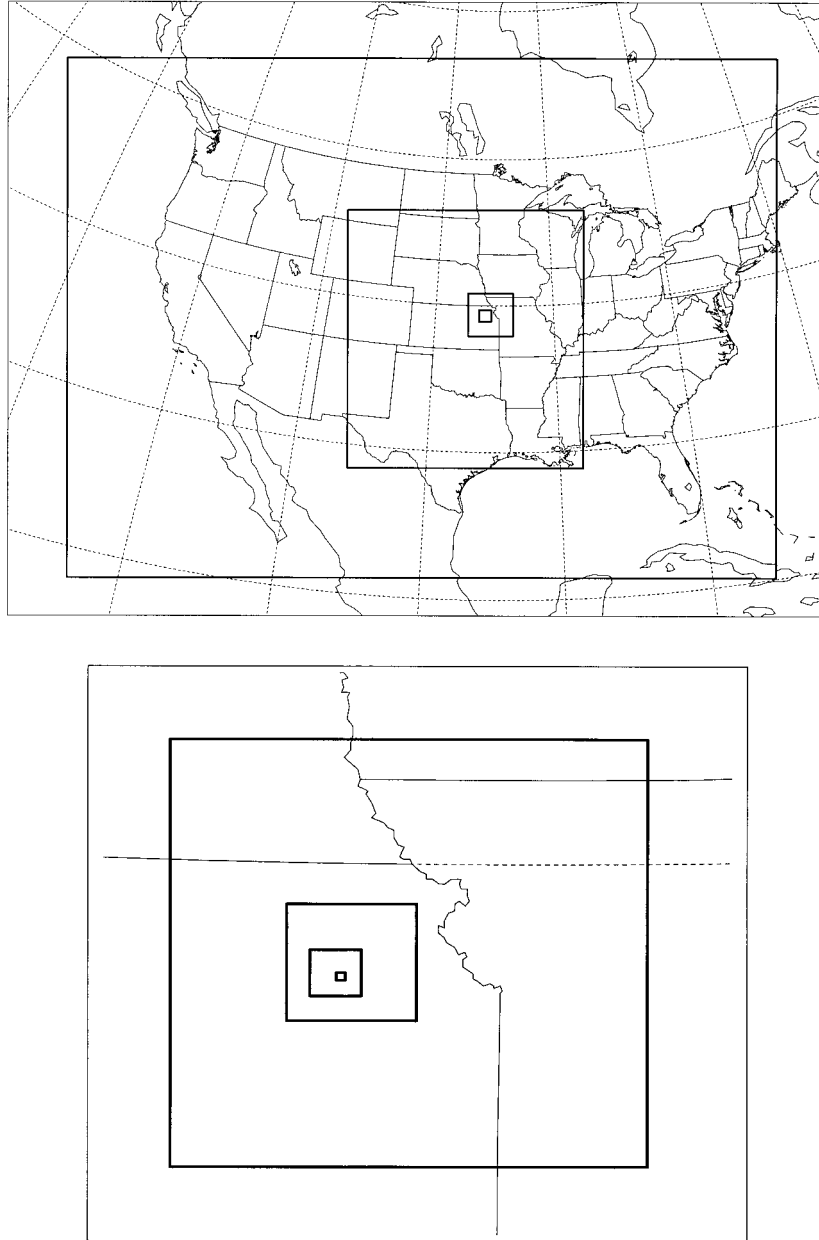
FIG. 5. Grid configuration for the 30 Jun 1993 case (grid boundaries are denoted by the bold lines). The top figure shows the positions of grids 1–3 and the initial position of grid 4. The bottom figure shows the initial positions of grids 3–6. Grids 4–6 were moved during the simulation.

tion. They presented results from a weakly forced MCC simulation in which outflow boundaries and other mesoscale features were detectable in the data but were not sufficiently resolved in the conventional model initialization. The data were reanalyzed and some "bogus" soundings were created by modifying the observed soundings at low levels based on a subjective mesoscale analysis. These bogus soundings were then included in the initial conditions in order to better capture the three-dimensional mesoscale environment. They found that

the specification of a "mesoscale" initial condition that included features like outflow boundaries and mesoscale pressure and wind features greatly improved their simulation of a series of MCCs. The current simulation is a bit more complicated since the observed outflow boundary developed around 1800 UTC, when the simulation was already under way. To incorporate the outflow into the simulation, interior nudging was performed over a limited region on grids 1–3 from 1600 to 2000 UTC (Fig. 6). During the nudging process, the obser-
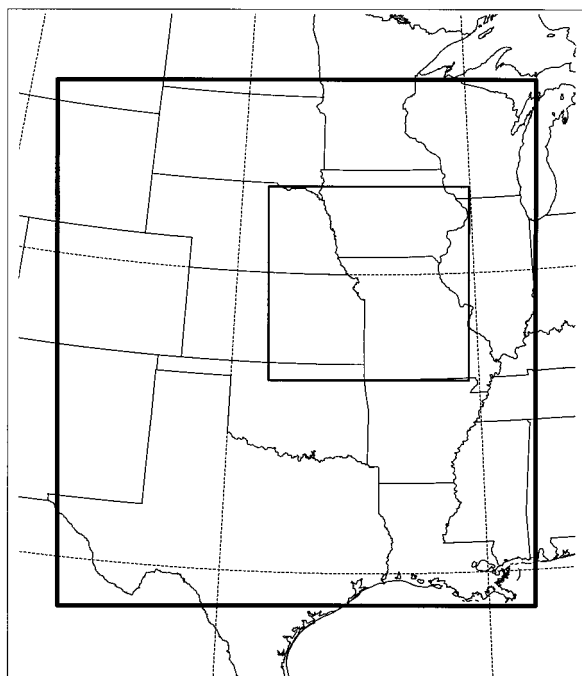
FIG. 6. Areal outline of the interior nudging region used in the simulation. The bold outline denotes the boundaries of grid 2. The finer outline denotes the boundaries of the interior nudging region used in the simulation.

vations are introduced into the model through an extra tendency in the model's predictive equations. The strength of the nudging tendency is inversely proportional to a nudging timescale that was chosen to be 1 h since the surface observations were 1 h apart. The strength of the nudging tendency dropped off quadratically to zero beyond the fourth horizontal grid point outside of the specified interior nudging region. The depth of the nudging region was ~1 km[1] since profiler data from the region indicated that the outflow depth was around 1 km. Because thermodynamic data were available only at the surface, the hourly surface data were allowed to influence the thermodynamic fields through the depth of the nudging region. Wind profiler data and surface winds were also used to approximate the winds throughout the depth of the nudging region. The outflow boundary (hereafter denoted as B1) weakened in time, but persisted throughout the duration of the simulation.

Grid 4 was added at 2000 UTC at which time the microphysics was also activated in the simulation. Grid 4 was initially centered over the intersection point between the stationary front and the outflow boundary since boundary layer moisture convergence on grid 3 was strongest in that region. Between 2125 and 2135

[1] The nudging weight was constant through the first eight model levels (up to 847 m), quadratically dropping off to zero by the twelfth model level (2 km).

UTC, the first storm began to develop near the intersection between the stationary front and B1 in northeast Kansas (similar to observations) where low-level convergence was strongest. Figure 7 shows the simulated low-level wind and condensate fields 20–30 min after convection developed on grid 4. Both the stationary front and B1 are visible in the wind field. The air south of the boundaries was potentially unstable, with Convective Available Potential Energy values of over 3000 J (kg)$^{-1}$. A typical model sounding taken just south of the developing convection is shown in Fig. 8. The shear vector turns clockwise with height below 800 mb with nearly unidirectional shear above this level.

The initial storm moved eastward along B1 during the first 20 min and at about 2148 UTC, the storm began to split in a manner similar to the horizontally homogeneous supercell simulations of Klemp and Wilhelmson (1978a,b), Thorpe and Miller (1978), Schlesinger (1980), and Wilhelmson and Klemp (1978, 1981) as shown in Fig. 9. The cyclonically rotating "right-moving" storm (hereafter denoted as S1) remained almost stationary, while the anticyclonic left-moving storm moved to the north and weakened rapidly.

Between 2148 and 2230 UTC, S1 moved eastward along B1 at 5–8 m s^{-1}, and additional convection began to develop northwest of S1. This convection was rooted in a convergence zone above the surface created by southerly flow associated with a low-level jet overrunning B1. The new convection first originated immediately northwest of S1 and then developed westward along the convergence zone until 2253 UTC when convective cells extend along an entire east–west line between S1 and the stationary front.

By 2307 UTC, two convective cells became dominant; S1, and the cell that developed farthest west along the elevated convergence zone (hereafter denoted as S2) as shown in Fig. 10. Cell S1 began to take on characteristics of an HP supercell as the condensate field developed an S-shaped structure. Significant precipitation was falling to the west and southwest of the updraft, which is characteristic of HP supercells, with precipitation rates approaching 12 (cm) h^{-1}. By 2334, both storms exhibited supercell characteristics including mid-level rotation and "hook echo" patterns in the condensate fields (not shown).

From 2300 to 0000 UTC, S2 appeared to undergo a slow "splitting" process somewhat similar to S1. At levels below 3.5 km, the condensate field associated with S2 elongated into two distinct maxima: one to the north and another to the south. Above 4 km, the southern maximum became dominant. The updraft was split by a downdraft below 4 km, with the southern updraft (right-moving storm) rotating cyclonically, and the northern updraft (left-moving storm) rotating anticyclonically as shown in Fig. 11 (hereafter the left-moving storm will be denoted as S3). However, S2–S3 did not split in the classic sense in that the condensate fields associated with the updrafts did not completely separate
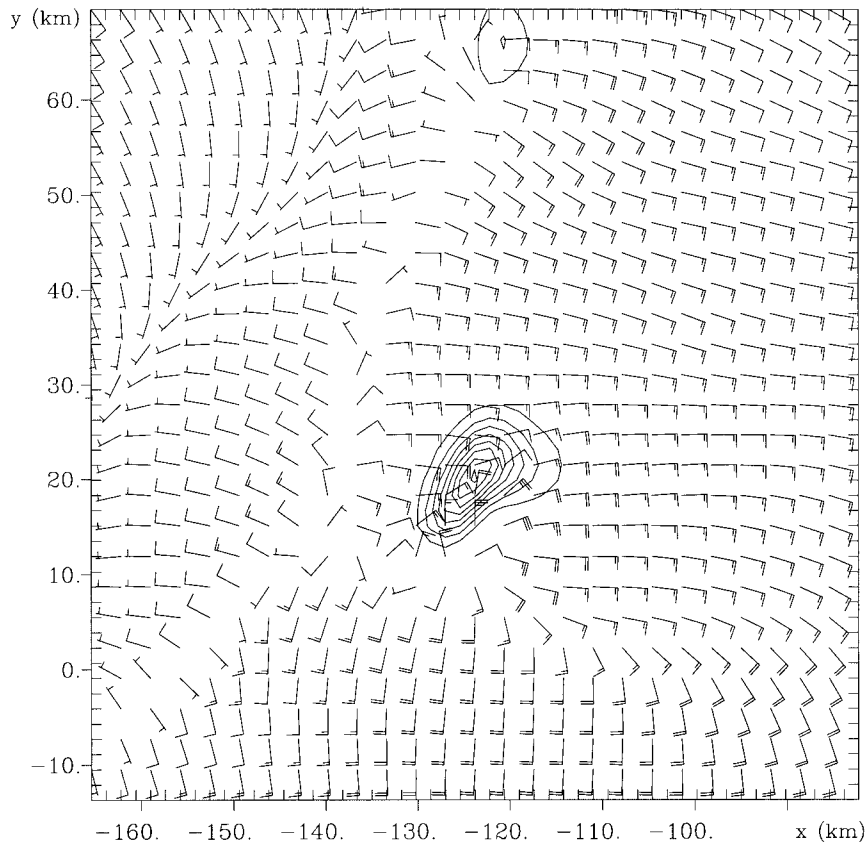
FIG. 7. Winds and condensate mixing ratio 38 m above the surface at 2148 UTC, 20–30 min after convection was initiated on grid 4. Wind barbs are plotted at every other model grid point. The short (long) flag on the wind barb represents 2 m s^{-1} (4 m s^{-1}). Condensate mixing ratio is contoured every 0.25 g kg^{-1}.

at mid-/upper levels until about 0027; instead, the condensate field elongated in the north–south direction as S3 moved slowly northeast, and S2 discretely propagated to the southeast. The left-moving storm (S3) was weaker than the right mover (S2), but remained identifiable throughout the duration of the simulation.

Grids 5 and 6 were added in the simulation at 0000 UTC 1 July. Originally only grid 5 was added at this time to better capture the system's transition into a bow echo, but the low-level wind fields showed evidence of rotation developing around 0015 UTC. As a result, grid 6 was also added at 0000 UTC over the region where rotation developed at low levels on grid 5. Grid 5 captured the evolution of the supercell in more detail as well as some of the gross features of the simulated tornadoes. Between 0000 and 0100 UTC, some large structural changes took place in S1. As shown in Fig. 12, S2 continued to discretely propagate southeastward from 0000 to 0015 UTC until it merged with the southern portion of S1's flanking line between 0015 and 0021. This resulted in one large continuous updraft in which S2 lost many of its supercell characteristics. The merger of the two updraft regions produced a sudden increase in the depth and strength of convection in the region

surrounding the merger point between 0015 and 0019 UTC. At $z = 6.1$ km on grid 5, updrafts increased from 16 to 18 m s^{-1} at 0013:30 UTC to 28–32 m s^{-1} at 0019, with maximum updrafts reaching 56 m s^{-1} near the tropopause (simulated storm tops reached approximately 16–17 km). The sudden and rapid increase in convective intensity after cell merger has been observed by Simpson and Woodley (1971), Lemon (1976), and Houze and Cheng (1977). The cell merger and the associated updraft intensification may have played a role in the development of the first tornado in the simulation, which developed along the flanking line of S1 at this time. Observations of tornadogenesis following the interaction between a supercell and other convection have been documented by Wolf (1998), Sabones et al. (1996), Goodman and Knupp (1993), and Bullas and Wallace (1988). The connection between cell merger and tornadogenesis in this case will be discussed further in Part II. As quickly as the convection intensified near the updraft merger point, it weakened, and by 0021 UTC updrafts in the region were 14–18 m s^{-1} at $z = 6.1$ km. All during this time period, S1 (which now dominates the northern portion of the storm) retained its supercell characteristics. Thus the two storms merged into a single
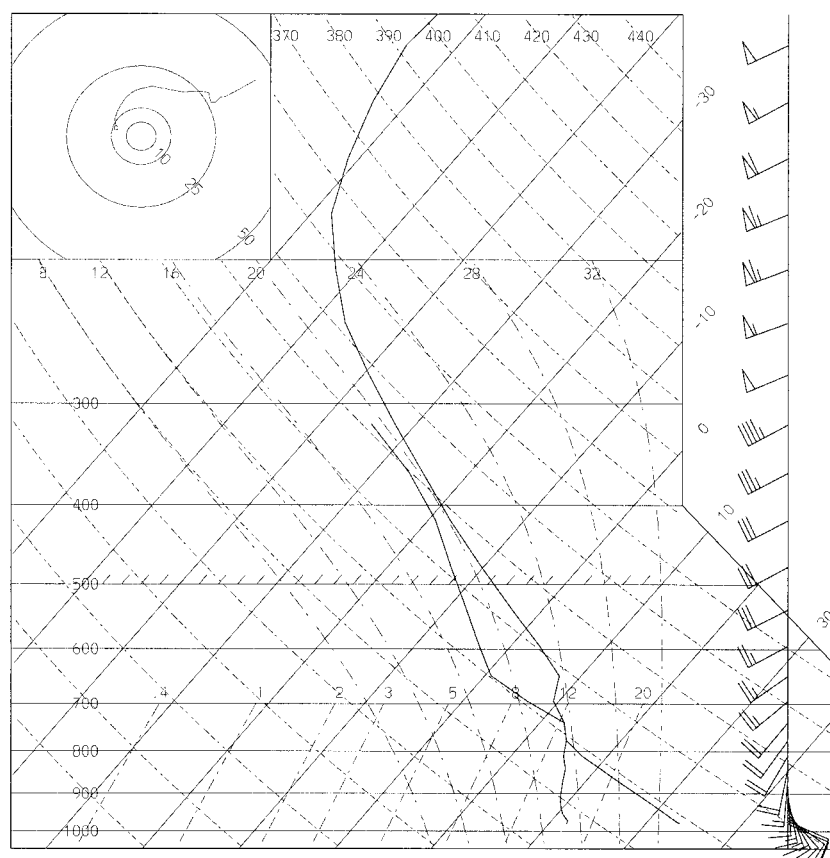
FIG. 8. A vertical sounding and hodograph taken at 2040 UTC on grid 4. Convection began to develop in the simulation just north of this point about 20 min later. The long (short) flag on the wind barbs denotes a wind speed of 10 kt (5 kt).

storm containing one mesocyclone at the northern end of the line (associated with S1) and a large flanking line[2] extending south and west. Although the cells along the flanking line were associated with significant values of positive vertical vorticity, they did not display obvious signs of rotation.

At the same time the strong updrafts were weakening in the merger region (0020–0030 UTC), the pressure dropped over an elongated area surrounding the convective band. The pressure drop occurred over a large depth of the troposphere and was associated with a gravity wave that was emitted from the storm between 0020 and 0030 UTC as shown in Fig. 13. The gravity wave appeared to be generated by the rapid intensification and weakening of convection associated with the updraft merger since the largest wave amplitude originated from that region of the storm. The wave moved east-southeast away from the storm at about 31 m s^{-1} and extended through the depth of the troposphere with the largest amplitude (both in the pressure and vertical velocity

fields) occurring at midlevels. Figure 14 shows a time series of the simulated wind and pressure fields at a point originally east of the storm. In the middle troposphere, the wave passage is marked by a pressure drop of 1.5 mb, and upward motion of 5–6 m s^{-1}. Like the pressure drop associated with the wave, the upward motion also extended through most of the troposphere. Although the upstream propagating wave was also visible at later times, the downstream propagating wave had much larger amplitude in both the vertical motion and pressure fields.

Between 0010 and 0040 UTC, several condensate and vertical vorticity maxima developed along the central and southern portion of the flanking line and moved north-northeastward along the gust front in time, eventually merging with the mesocyclone (Figs. 12 and 15). A similar evolution was noted by Lemon (1976) and Barnes (1978a,b), who used radar observations to document HP supercells where cells in the flanking line moved toward and merged with the main storm updraft. During and after the merger events, the simulated mesocyclone grew in size and intensified, both with respect to increased maximum vertical vorticity and lower pressure. With time, the storm evolved into a rotating com-

---

[2] The term ''flanking line'' in this study is referring to convective cells along the large outflow boundary extending south of the mesocyclone.
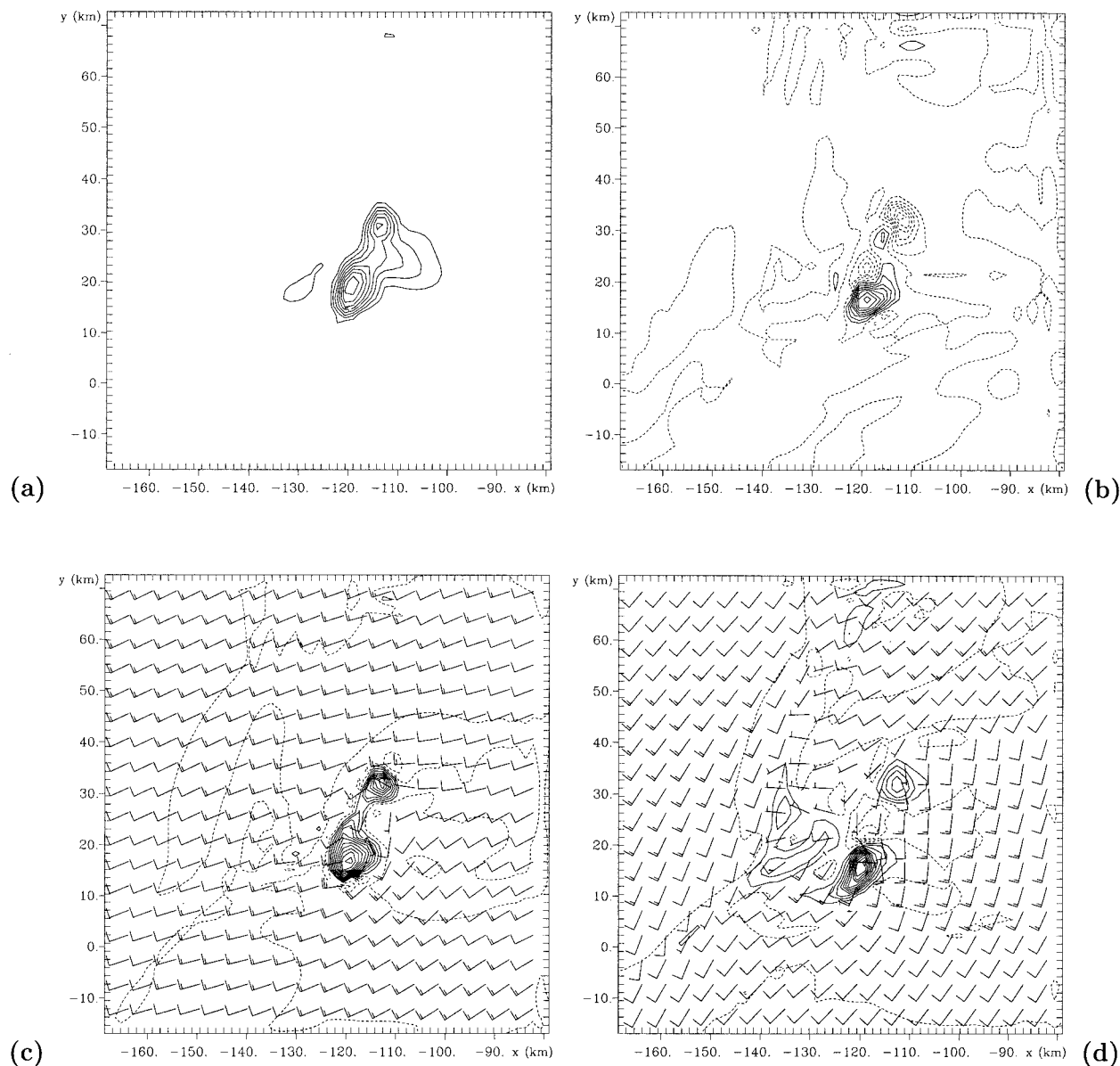
FIG. 9. Model fields on grid 4 at 2200 UTC shortly after the first storm splits. (a) Condensate field at $z = 4.3$ km, (b) vertical vorticity field at $z = 4.3$ km, (c) vertical velocity field overlayed with horizontal winds at $z = 4.3$ km, (d) vertical velocity field overlaid with horizontal winds at $z = 1.7$ km. Condensate mixing ratio is contoured every 1 g kg^{-1}. Vorticity contour interval is 0.001 s^{-1}. Vertical velocity is contoured every 2 m s^{-1} at $z = 4.3$ km, and every 1 m s^{-1} at $z = 1.7$ km. Wind barbs are plotted at every third grid point. The short (long) flag on the wind barb represents 5 m s^{-1} (10 m s^{-1}). Dashed contours indicate negative values.

ma-head structure (Fig. 12). This finding supports the idea proposed by Lemon (1976) that the flanking line could be an important vorticity source for some rotating storms. Also during this time period, negative vertical vorticity developed along the southern end of the storm behind the convective line. Between 0030 and 0040 UTC, two distinct counterrotating vortices emerged at midlevels in the storm as can be seen in Figs. 15d,e. These counterrotating vortices are often referred to as "book-end vortices" and are a common feature of bow

echoes (Rotunno et al. 1988; Schmidt 1991; Weisman 1993; Skamarock et al. 1994).

During the time period from 0030 to 0040 UTC, the winds behind the gust front accelerated eastward over a large depth of the troposphere from the surface up to about 7 km. As this occurred, the positive vertical vorticity along the gust front increased at low levels and the gust front surged eastward (not shown). This marked the storm's transition into a bow echo or rotating comma-head structure. Recall that this is one of the possible
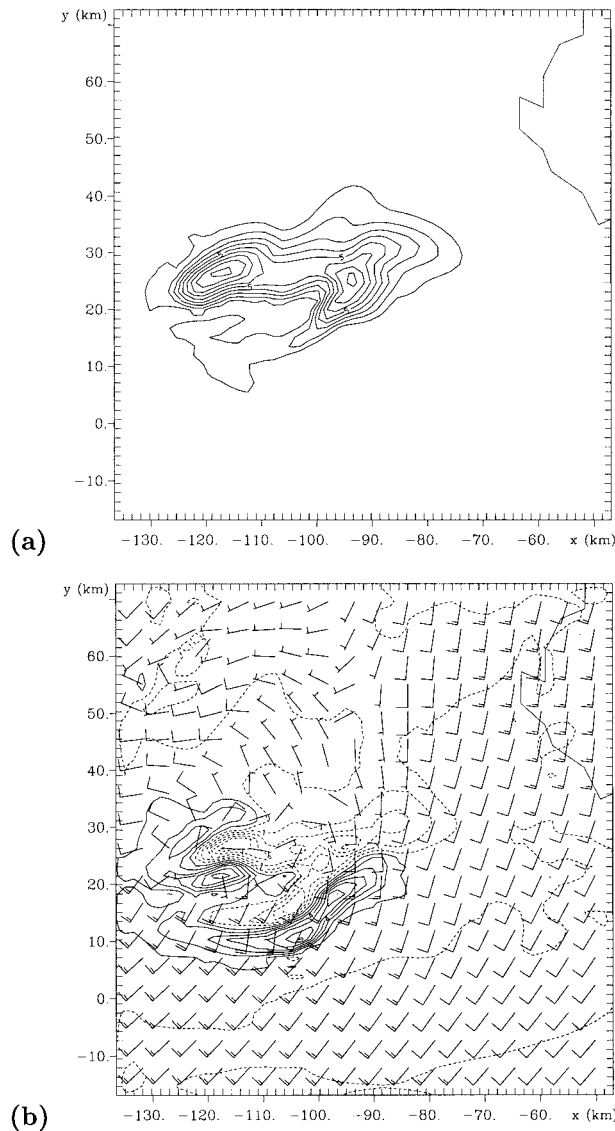
(a)

(b)

FIG. 10. Continued storm evolution on grid 4 at 2307 UTC. (a) Condensate field at $z = 4.3$ km, (b) vertical velocity field overlayed with horizontal winds at $z = 1.7$ km. Condensate mixing ratio contour interval is 1 g kg^{-1}. Vertical velocity is contoured every 1 m s^{-1} (dashed contours indicate negative values). Wind barbs are plotted at every third grid point. The short (long) flag on the wind barbs indicates 5 m s^{-1} (10 m s^{-1}).

FIG. 11. Condensate field overlayed with wind barbs at 0000 UTC at $z = 2.9$ km on grid 5. Condensate mixing ratio is contoured every 0.5 g kg^{-1}. The short (long) flag on the wind barbs denotes a speed of 5 m s^{-1} (10 m s^{-1}). Wind barbs are plotted at every other grid point.

life cycles of an HP supercell as documented by Moller et al. (1990). The acceleration near the surface was particularly large along the south side of the mesocyclone where wind speeds reached 28 m s^{-1} between 0033 and 0037 UTC on grid 5.

After 0040 UTC, the storm updrafts weakened considerably as the high θ_e inflow into the mesocyclone was cut off, and the convection along the central portion of the bow dissipated. The low pressure center associated with the mesocyclone began to fill, and the areal extent of the rotation broadened and the rotation weakened. The simulation was terminated at 0100 UTC 1
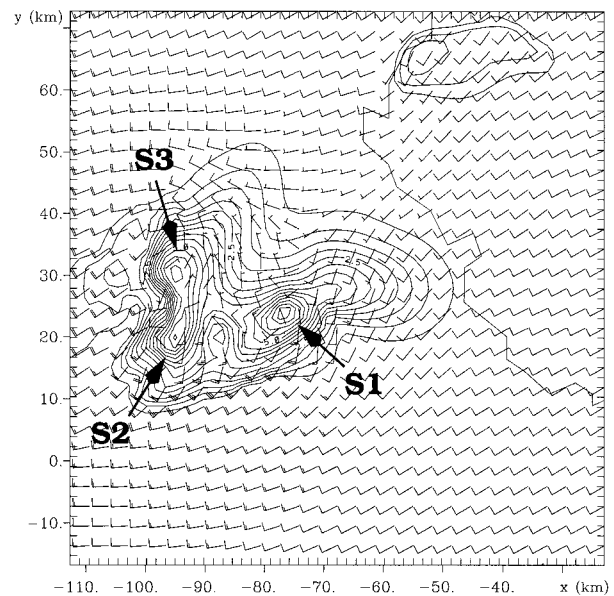
July since the simulated storm weakened and the observed storm became part of a large and well-organized squall line extending from northeast Kansas into eastern Iowa.

5. Analysis of the bow echo transition

It is not known why some HP supercells become bow echoes. However, observational studies by Moller et al. (1994) have shown that HP supercells in close proximity to other convection are more likely to follow the bow echo life cycle. Wolf (1998) documented a case in eastern Oklahoma in which a bow echo interacted with the southern edge of a supercell. Following the merger, the original bow echo weakened while the supercell retained its identity and severity, and it evolved into an HP supercell that had a "comma-shape" echo appearance. Changes in the supercell structure included: the development of a 15–20-km-wide mesocyclone circulation that "engulfed" the original 5–8-km-wide mesocyclone, the development of a rear inflow notch south of the mesocyclone, and the formation of a reflectivity minimum near the center of the mesocyclone circulation. Sabones et al. (1996) also documented two cases in which outflow producing convection interacted with the southern edge of an existing supercell. In both cases, the supercell evolved into a rotating comma-head structure. These studies suggest that the interaction between supercells and other convection may play an important role in the transition of some supercells into HP supercells/bow echoes.

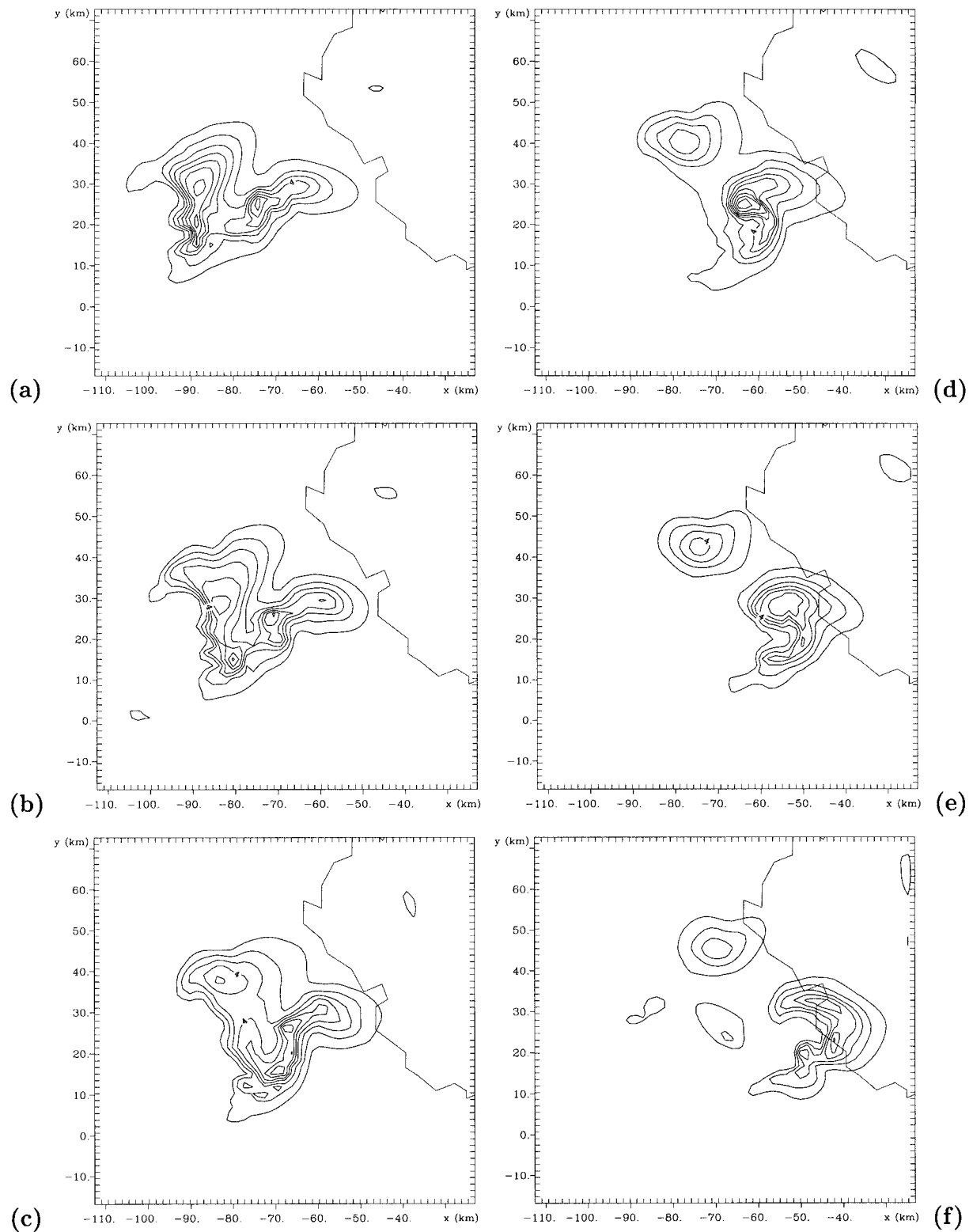The model simulation presented above suggests that

FIG. 12. Evolution of the condensate field (contour interval 1 g kg^{-1}) at 2.5 km above the surface on grid 4 at (a) 0010:30 UTC, (b) 0019:30 UTC, (c) 0030 UTC, (d) 0040:30 UTC, (e) 0049:30 UTC, and (f) 0100 UTC. The line running throught the northeast corner of the grid is the Kansas–Missouri border.
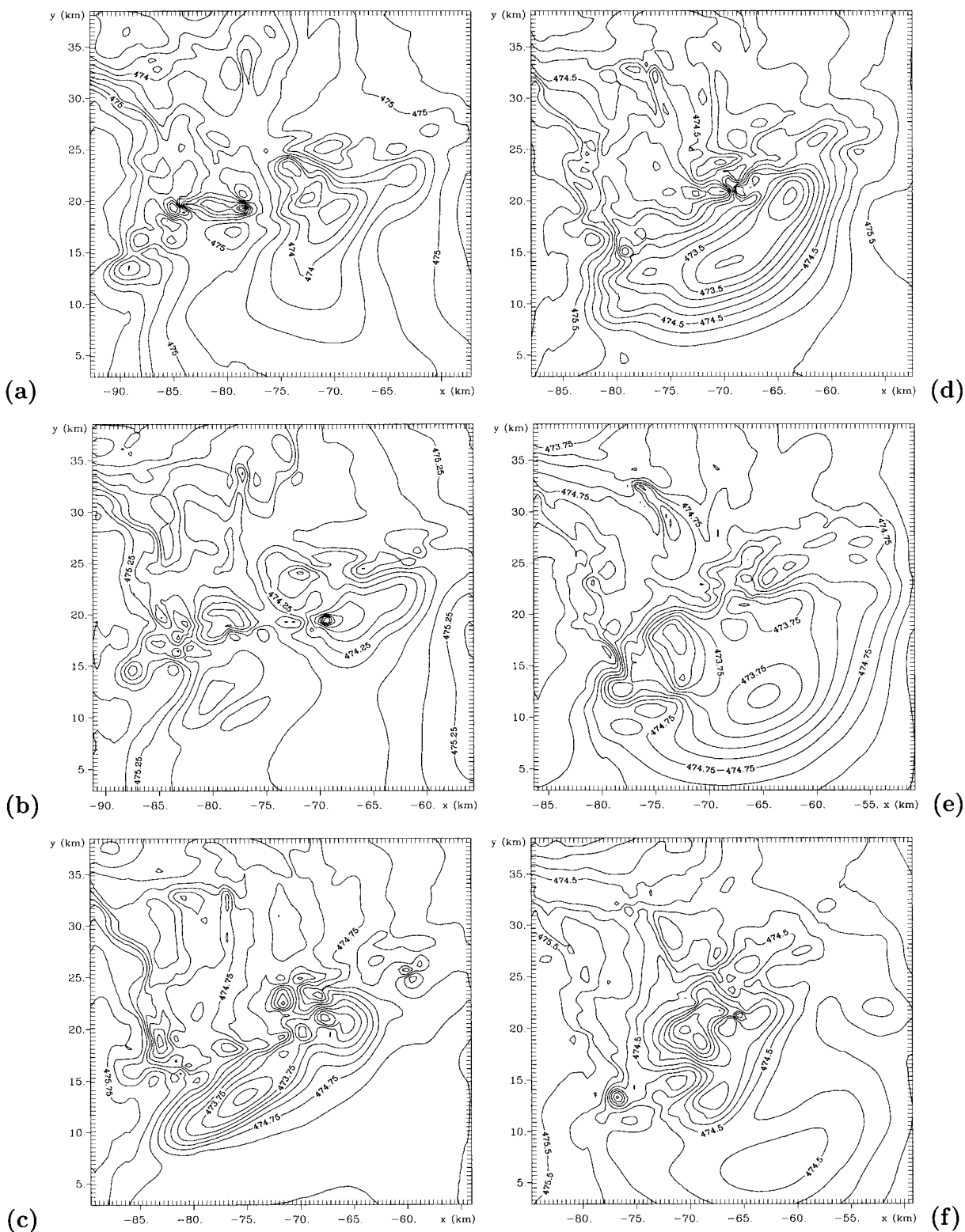
FIG. 13. Evolution of the pressure field (contour interval 0.25 mb) on grid 4 6.1 km above the surface at (a) 0013:30 UTC, (b) 0016:30 UTC, (c) 0019:30 UTC, (d) 0022:30 UTC, (e) 0025:30 UTC, and (f) 0028:30 UTC. Note the large gravity wave that propagates away from the storm between 0020 and 0030 UTC.
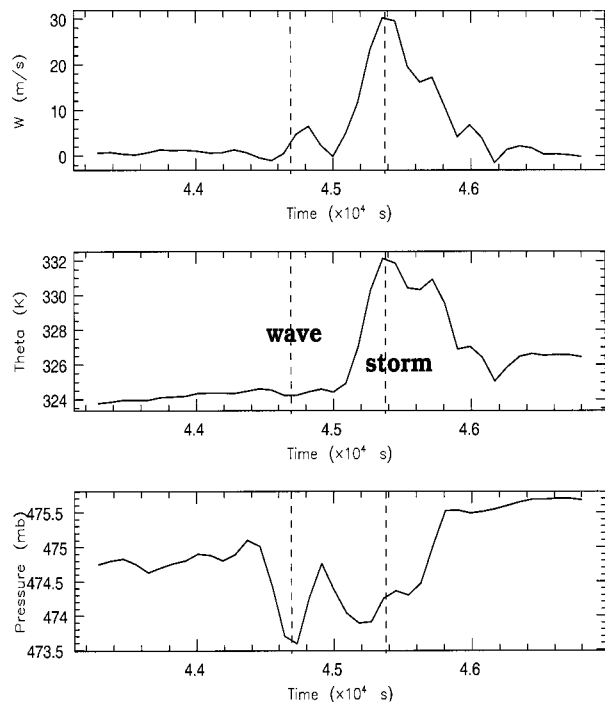
FIG. 14. Time series of vertical motion, potential temperature, and pressure at $z = 6$ km at a point on grid 4 that is downstream of the storm when the gravity wave is emitted. The gravity wave passes the point between approximately 0020–0030 UTC (44 400 s–45 000 s). The storm passes the point around 0037 UTC (45 400 s).

two physical processes may play an important role in the transition of the HP supercell into a bow echo: 1) the intensification of the low-level cold pool, 2) intensification and expansion of the mesocyclone. Both of these events occurred immediately following the merger of S2 with the flanking line of S1. In this section, the transition of the simulated HP supercell into a bow echo will be investigated further, including the role that cell interaction/merger plays in the transition.

a. Effects of cell merger on cold pool evolution

Previous idealized modeling studies of bow echoes have demonstrated the importance of low-level cold pools in the transition of individual thunderstorms into squall lines and bow echoes (Rotunno et al. 1988; Weisman et al. 1988; Lafore and Moncrieff 1989; Fovell and Ogura 1989; Skamarock et al. 1994). In these studies, the cold pool strengthens systematically in time as new cells develop and begin precipitating along the leading edge of the cold pool created by previous convection. However, both observational and modeling studies of cloud (updraft) mergers have shown that precipitation increases significantly following merger (Simpson and Woodley 1971; Tao and Simpson 1984; Westcott 1984). In an observational study by Lee et al. (1992a,b), a sudden increase in precipitation rate preceded the development of a wet microburst. The microburst en-

hanced the pressure gradient across the gust front, leading to an acceleration of the gust front. The storm also developed a bow echo structure following microburst formation.

Recall that S2 merged with the convection along the flanking line of S1 between 0015 and 0021 UTC, approximately 10–15 min before the storm began to evolve into a bow echo. Between 0019:30 and 0025:30 UTC, the precipitation rate increased significantly in the region surrounding $x = -77$ km, $y = 13$ km where the merger had occurred 5–10 min before as shown in Fig. 16. This time corresponded to the collapse of convection in the region, and the weakening of S2 as it became part of the flanking line of S1. An increase in precipitation rate prior to bow echo development is consistent with the results of Lee et al. (1992a,b) who observed a similar evolution just prior to the development of a single-cell type bow echo. The precipitation maximum moved northeastward behind the gust front (paralleled by the movement of the mesohigh) and increased from 170 to 190 mm (h)$^{-1}$ between 0025:30 and 0036 UTC. After 0045 UTC, maximum precipitation rates reached 210 mm (h)$^{-1}$ along the southwest quadrant of the rotating comma-head structure (not shown).

A strong mesohigh developed behind the gust front in response to the sudden increase in precipitation and evaporative cooling as shown in Fig. 17. The horizontal pressure gradient increased over a large area along the gust front around 0025 UTC as the pressure ahead of the gust front dropped in association with the gravity wave being emitted from the storm at this time. The center of high pressure behind the gust front moved northeastward and expanded in area during the next 5 min in response to the increasing precipitation rate shown in Figs. 16 and 17c. Vertical cross sections taken through low levels in the storm indicated that the depth of the cold air also increased from 1 to 2 km in the region of the expanding high pressure. During this time the horizontal pressure and temperature gradients continued to strengthen in the immediate vicinity of the gust front. Between 0028:30 and 0030 UTC, the gust front accelerated rapidly eastward and began to wrap around the mesocyclone. The vertical vorticity along the flanking line also doubled due to increased tilting and convergence along the leading edge of the outflow. (Note that grid 5 was moving during this time period so the x and y positions are changing along the axes in time.)

By 0036 UTC, the high pressure area behind the gust front weakened as shown in Fig. 17d. Vertical cross sections taken through low levels in the storm indicated that the weakening high pressure was associated with the collapse of the cold pool, as the cold air spread out along the surface. Although the pressure behind the gust front decreased, the horizontal pressure gradient along the gust front was still large, and the gust front continued to move rapidly eastward and wrap around the mesocyclone through 0055 UTC.
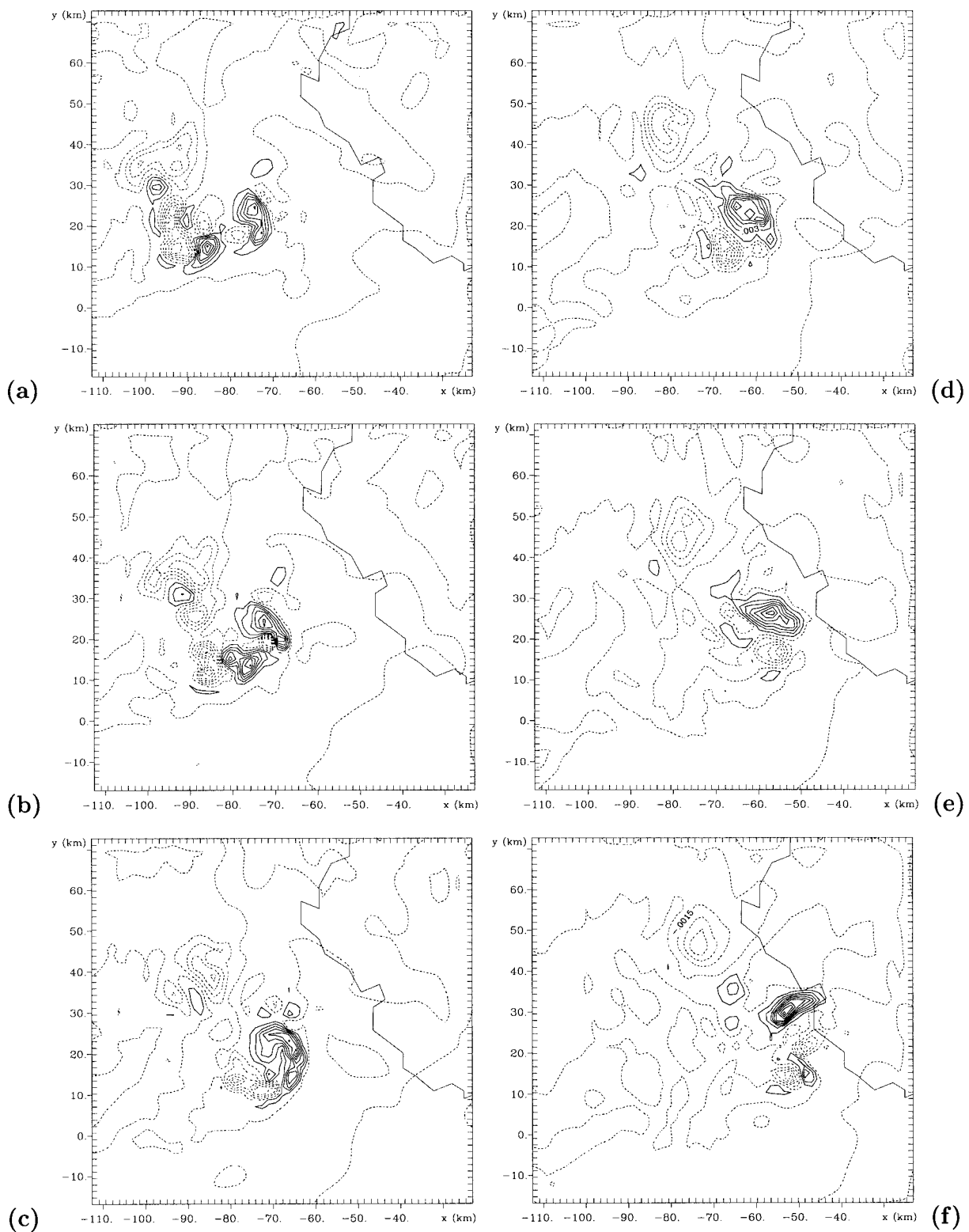
FIG. 15. Evolution of the vertical vorticity field (contour interval 1.5×10^{-3} s^{-1}) at 2.5 km above the surface on grid 4 at (a) 0010:30 UTC, (b) 0019:30 UTC, (c) 0030 UTC, (d) 0040:30 UTC, (e) 0049:30 UTC, and (f) 0100 UTC. Dashed contours indicate negative values.
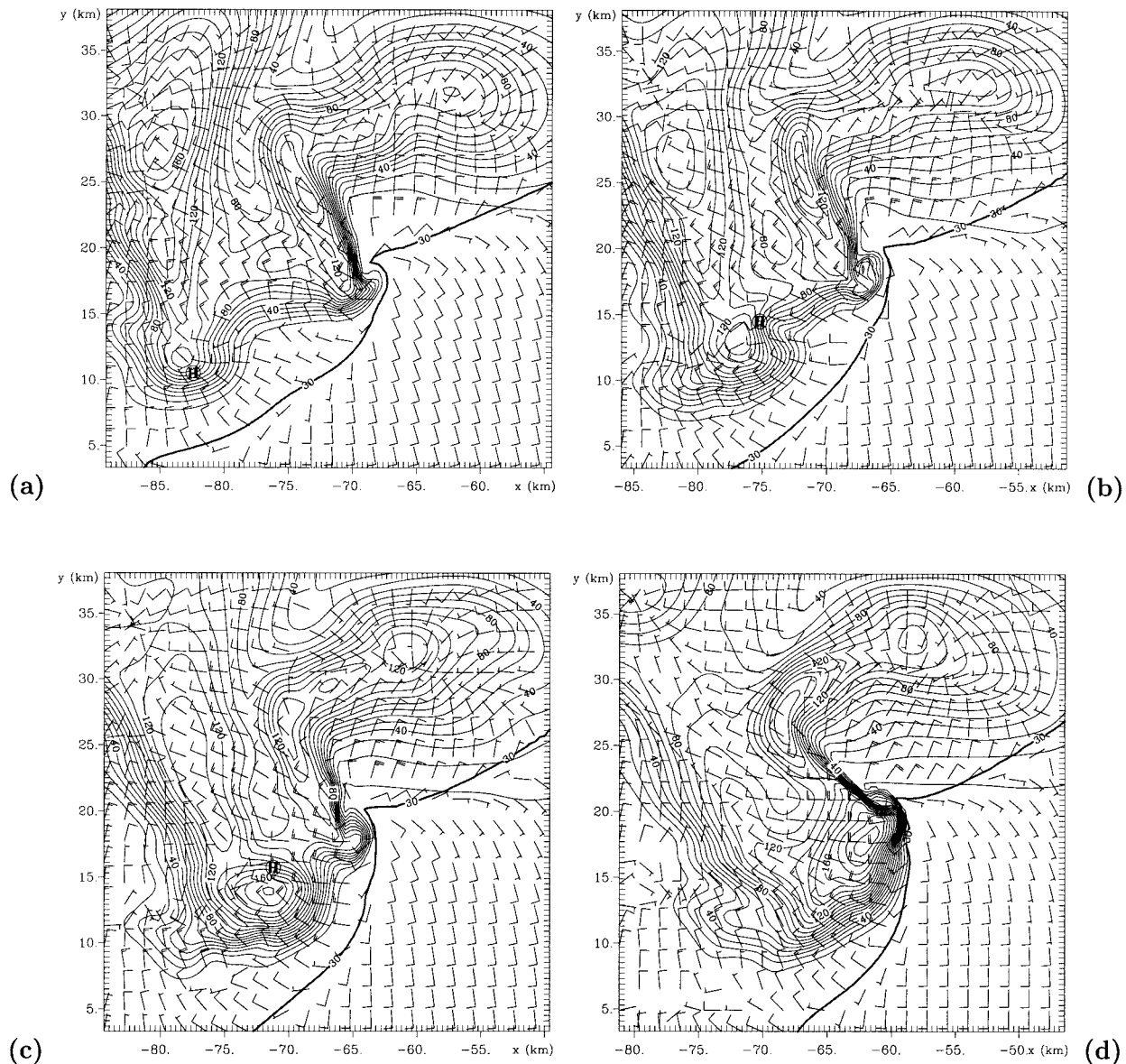
FIG. 16. Horizontal cross sections showing the precipitation rate (in mm h^{-1}) overlaid with the horizontal winds at $z = 38$ m on grid 5 at (a) 0019:30 UTC, (b) 0025:30 UTC, (c) 0030 UTC, and (d) 0036 UTC. The contour interval is 10 mm h^{-1}. The bold line denotes the 30°C isotherm, which is close to the leading edge of the gust front. The circled H in (a), (b), and (c) denotes the center of a region of high pressure behind the gust front. Wind barbs are plotted at every fourth model grid point. The short (long) flags on the wind barbs denote a wind speed of 5 m s^{-1} (10 m s^{-1}).

b. Development of the rear inflow

Previous studies have shown that the rear inflow in squall lines develops in response to upshear-tilted updrafts in the convective line, which occur as a result of the strengthening of the low-level cold pool (Rotunno et al. 1988; Weisman et al. 1988; Lafore and Moncrieff 1989; Fovell and Ogura 1989; Skamarock et al. 1994). A similar evolution is seen along the flanking line in the current simulation as the HP supercell goes through the bow echo life cycle. Vertical cross sections taken through the center of the flanking line on grid 5 at sev-

eral successive times prior to and during the transition are shown in Fig. 18. Just prior to the transition around 0030 UTC, the updrafts along the center of the line began to lean toward the west (upshear) with height—especially in the lowest 7 km above the surface (see Figs. 18a,c). This was the same time that the gust front rapidly accelerated eastward as the low-level cold pool and mesohigh at the surface intensified. The updrafts continued to lean westward with height until shortly after 0040 UTC when the updrafts weakened significantly and became more upright as shown in Fig. 18e,
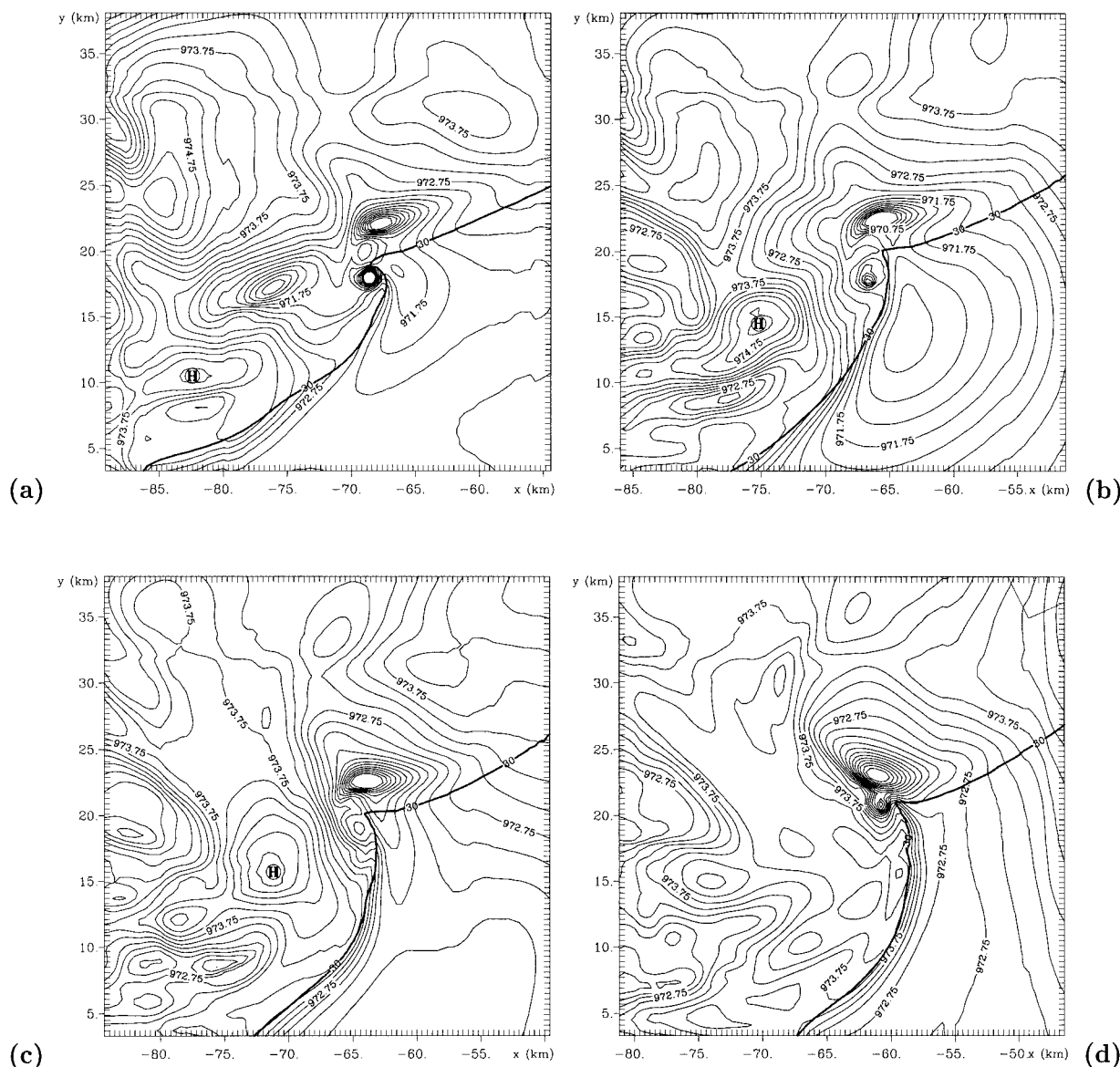
FIG. 17. Horizontal cross sections showing the pressure field (in mb) at $z = 38$ m on grid 5 at (a) 0019:30 UTC, (b) 0025:30 UTC, (c) 0030 UTC, and (d) 0036 UTC. Contour interval for the pressure is 0.25 mb. The bold line denotes the 30°C isotherm, which is close to the leading edge of the gust front. The circled H in (a), (b), and (c) denotes the center of a region of high pressure behind the gust front. The intense area of low pressure at $x = -68$ km, $y = 18$ km in (a) is the first tornado-like vortex in progress.

eventually leaning eastward (downshear) with height as the low-level cold pool weakened. Although the storm did not have an extensive rear inflow jet extending far behind the convective line as is the case with many mesoscale convective system (MCS) bow echoes, the storm did have elevated strong storm-relative westerly winds extending westward 10–15 km behind the flanking line.

As the updrafts along the center of the bow leaned westward with height, an area of low pressure developed at midlevels behind the convective line. This can be seen in the vertical cross section of perturbation pressure taken through the center of the bow at 0031:30 UTC

(Fig. 19). Previous idealized modeling studies have shown that this pressure gradient develops in response to horizontal buoyancy gradients associated with the warm convective plume aloft (Lafore and Moncrieff 1989; Fovell and Ogura 1989; Weisman 1992, 1993), or equivalently, this configuration of the buoyancy field supports a minimum in the hydrostatic pressure field at midlevels (LeMone 1983; LeMone et al. 1984). This results in a strong horizontal pressure gradient along the back side of the storm that accelerates the flow into the storm in this region. Note the strong pressure gradient extends vertically from $z = 2$ km to $z = 6$ km and 10–15 km behind the leading edge of the convective line.
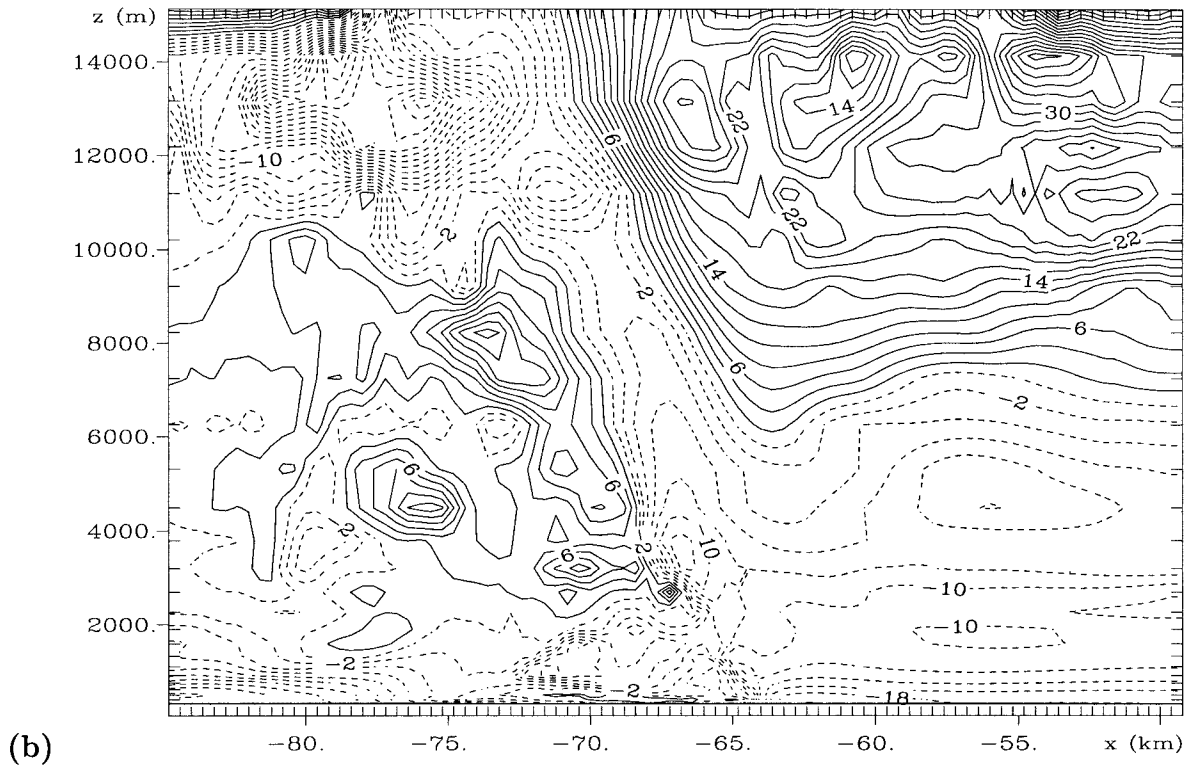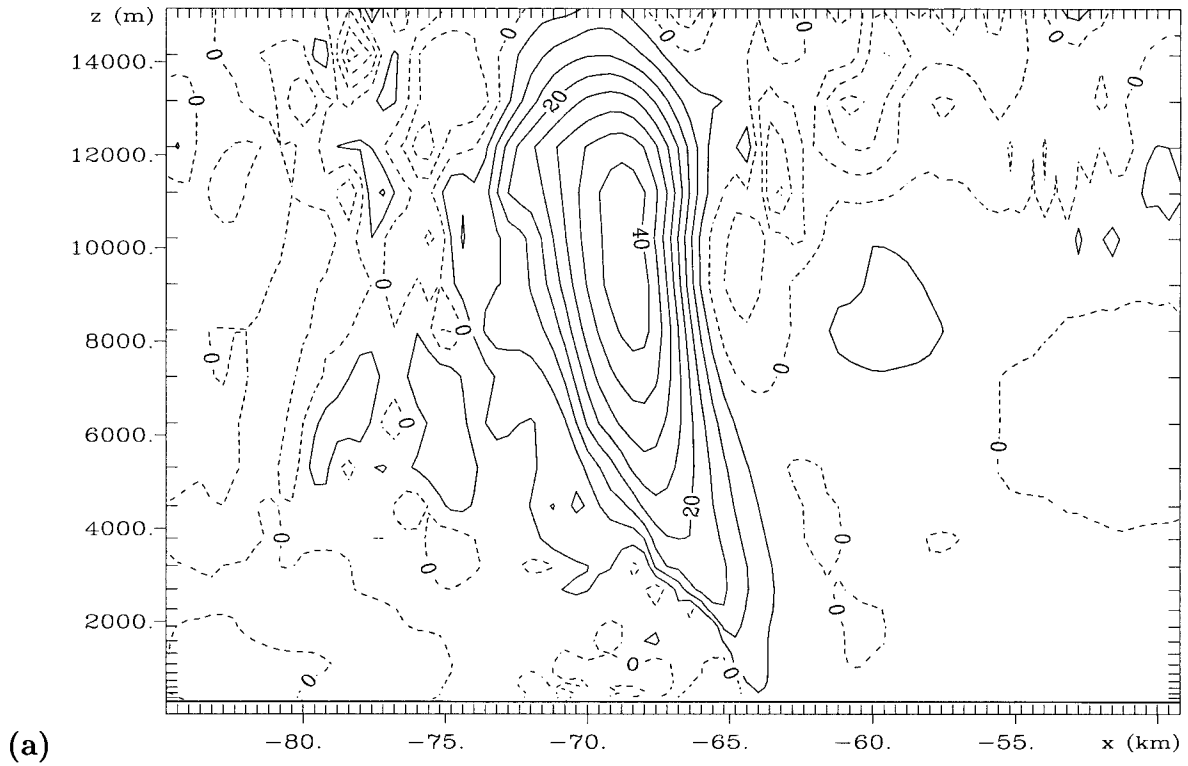
FIG. 18. Vertical cross sections (looking north) through the center of the bow echo on a subset of grid 5 (zoomed in on the storm). Shown is (a) vertical velocity, (b) storm-relative u at 0028:30 UTC, (c) vertical velocity, (d) storm-relative u at 0037:30 UTC (time of strongest winds), (e) vertical velocity, (f) storm-relative u at 0045 UTC. Contour interval is 5 m s^{-1} for the vertical velocity, 2 m s^{-1} for the storm-relative u wind component. Dashed contours denote negative values.

(c)
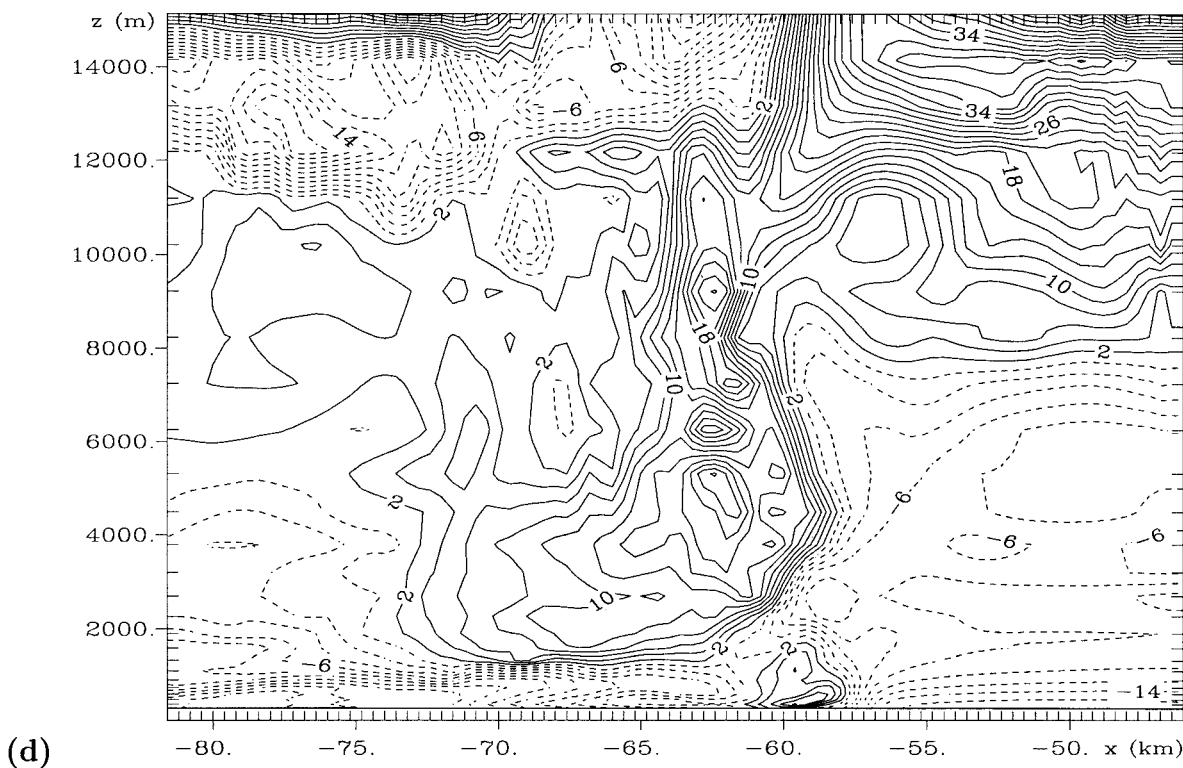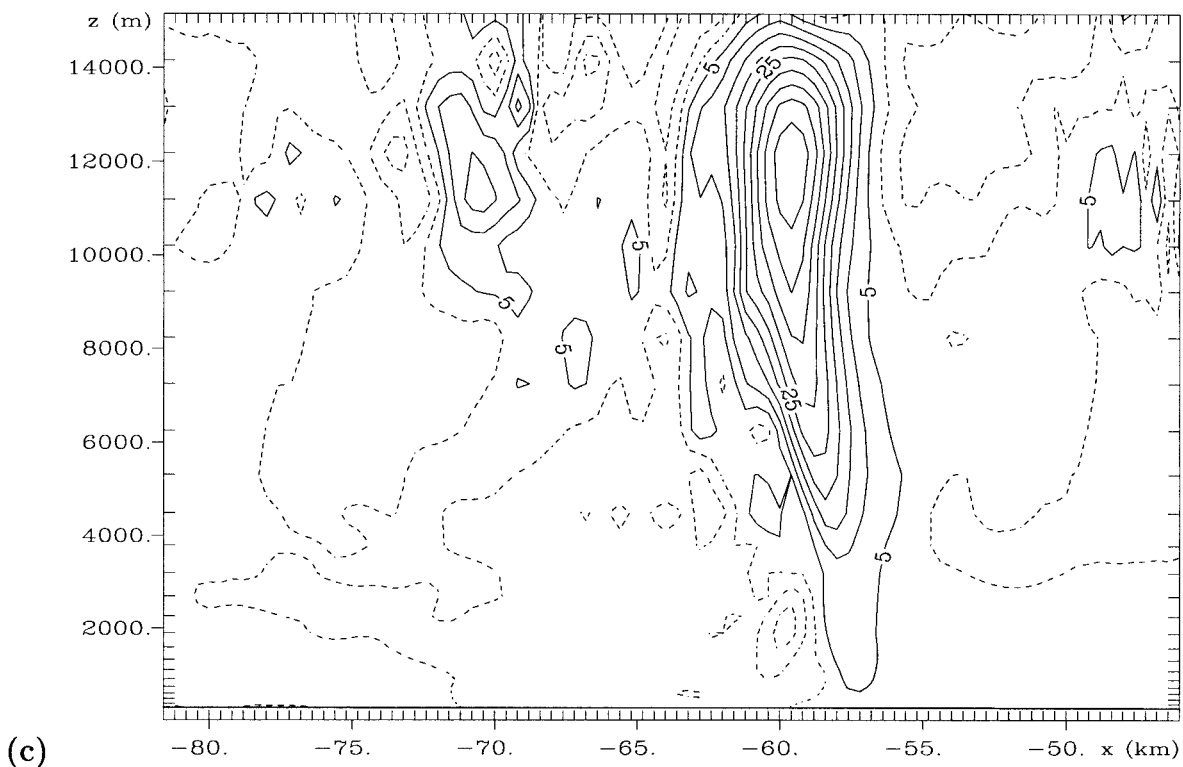

(d)

FIG. 18. (*Continued*)
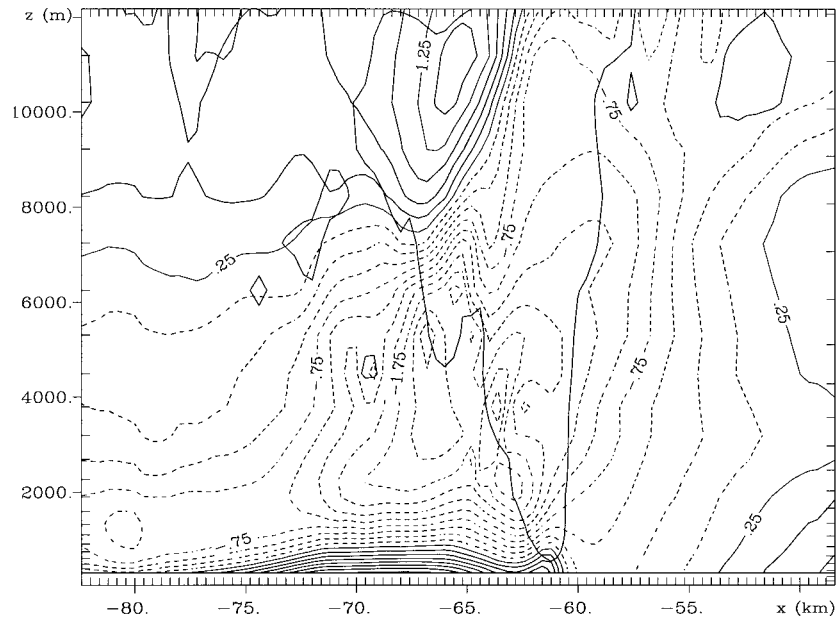
(e)

(f)

Fig. 18. (*Continued*)

FIG. 19. Vertical east–west cross section (looking north) of perturbation pressure (in mb) and vertical velocity at 0031:30 UTC on grid 5. Pressure is contoured every 0.25 mb. Dashed contours denote negative values. The bold solid line denotes the 5 m s^{-1} vertical velocity contour. Note the large horizontal pressure gradient between $z = 2$ km to $z = 6$ km along the west side of the storm.

This is the region where the strong inflow developed behind the storm.

The diagnostic perturbation pressure equation has been in previous studies to show that the pressure gradient that develops behind squall lines is a result of vertical buoyancy gradients created by upshear-tilted convective storms (Weisman 1993). The diagnostic perturbation pressure equation is given by (Rotunno and Klemp 1982, 1985):

$$-\boldsymbol{\nabla} \cdot (c_p \rho_0 \theta_{ov} \boldsymbol{\nabla} \pi)$$

$$= 2\rho_0 \left(\frac{\partial v}{\partial x} \frac{\partial u}{\partial y} + \frac{\partial u}{\partial z} \frac{\partial w}{\partial x} + \frac{\partial v}{\partial z} \frac{\partial w}{\partial y} \right)$$

$$+ \rho_0 \left[\left(\frac{\partial u}{\partial x} \right)^2 + \left(\frac{\partial v}{\partial y} \right)^2 + \left(\frac{\partial w}{\partial z} \right)^2 \right.$$

$$\left. - \frac{\partial^2 \ln(\rho_0)}{\partial z^2} w^2 \right] - \frac{\partial B}{\partial z}, \qquad (1)$$

where π is the perturbation Exner function, B is the buoyancy, and $\rho_0(z)$, $\theta_{ov}(z)$ are the base state density and virtual potential temperature, respectively. Equation (1) shows that there are three contributions or "forcing functions" to the diagnostic perturbation pressure: fluid shear [the terms in the first bracket on the right-hand side of (Eq. 1)], fluid extension (terms in the second bracket), and the vertical buoyancy gradient (the last term). The two contributions from velocity derivatives (shear and extension) are often grouped together into a "dynamic" contribution to perturbation pressure. To in-

vestigate the development of the rear inflow during the bow echo transition, the forcing terms on the right-hand side of Eq. (1) were calculated from the model wind and buoyancy fields to assess the importance of each of the contributions to the strong horizontal pressure gradient that developed along the back side of the storm. Since $-\boldsymbol{\nabla} \cdot (c_p \rho_o \theta_{ov} \boldsymbol{\nabla} \pi) \sim \pi$ (assuming π can be represented as a periodic function such as sine or cosine), we can get a rough picture of the pressure field resulting from each of the forcing functions.

A vertical cross section of the perturbation pressure and each of the forcing functions averaged over a distance of 6.5 km along the convective line at the center of the bow echo on grid 4 is shown in Fig. 20. During the early phase of the transition, the buoyancy forcing term was largely responsible for the distribution of the perturbation pressure field (and pressure gradient) behind the storm. A time series loop of the perturbation pressure field and the forcing terms showed that the horizontal pressure gradient (as shown in Fig. 20) intensified between 0024 and 0030 UTC due to the changing distribution and increasing magnitude of the buoyancy forcing as the convection began to lean upshear in response to the strengthening cold pool, consistent with the results of Weisman (1993). However, as the transition progressed, the dynamic forcing made an increasing contribution to the negative perturbation pressure behind the convective line.

By 0037:30 UTC, the dynamic and buoyancy forcing were comparable between $z = 3$–8 km as shown in Fig. 21. Examination of the forcing terms revealed that the
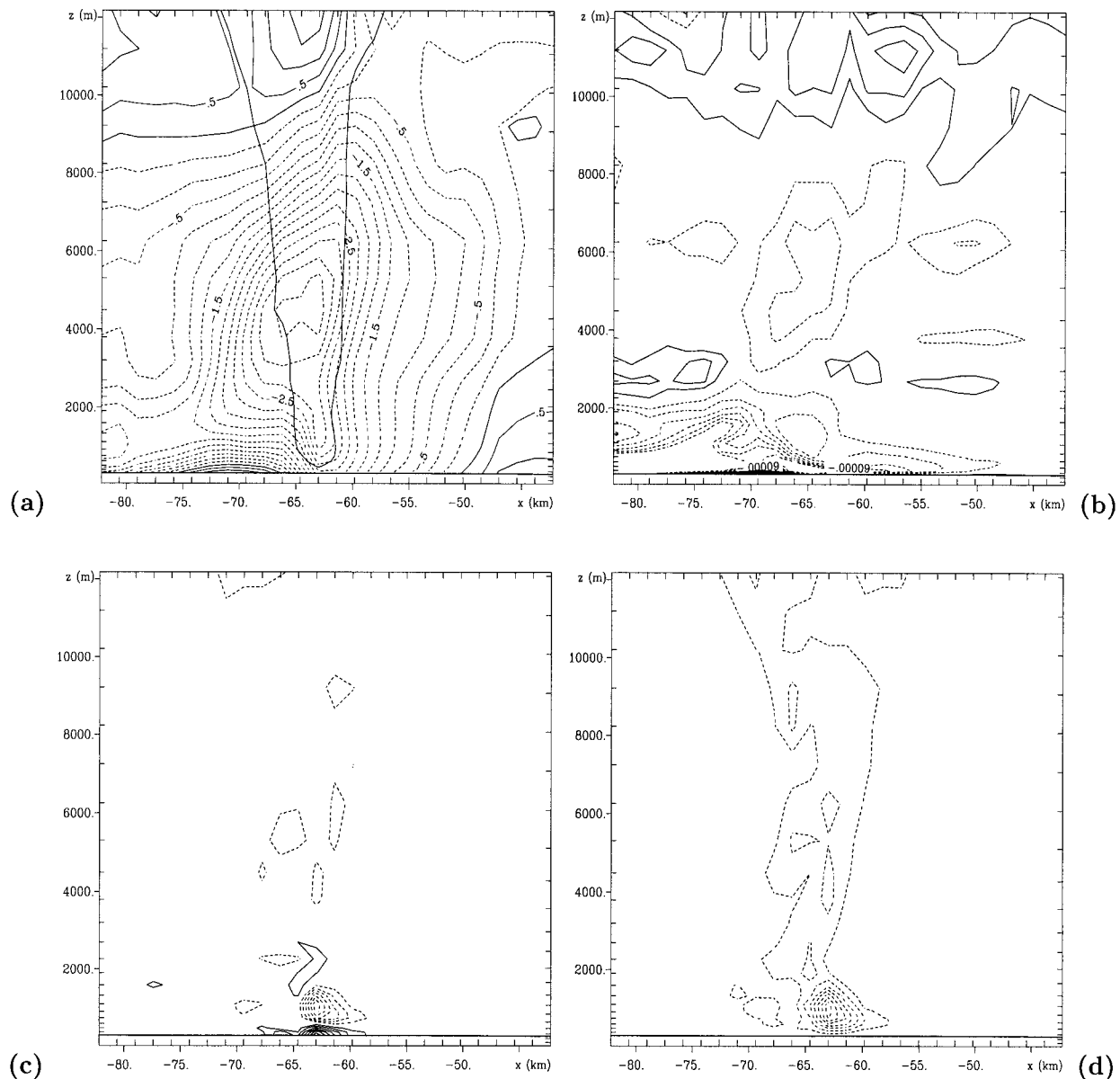
FIG. 20. Vertical cross sections of the along-line average of the forcing functions in the diagnostic perturbation pressure equation on grid 4 at 0033 UTC. Shown is (a) perturbation pressure (bold contour represents the 5 m s^{-1} vertical velocity contour), (b) buoyancy forcing, (c) dynamic forcing, and (d) shear forcing alone. Contour interval for the perturbation pressure is 0.25 mb. The contour interval for the forcing terms is 3×10^{-5} kg m^{-3} s^{-2}.

shear forcing was responsible for the negative region of dynamic forcing on the western edge of the convective line. The vertical vorticity nearly doubled between 0033 and 0036 UTC in a vertical sheet along the interface between the convective updraft and downdraft, corresponding with the intensification of the downdraft behind the convective line. This suggests that tilting was responsible for this sudden vorticity increase, which was confirmed from cross sections of the vorticity tendencies. Preliminary calculations suggest that the downdraft intensified as a result of dynamic (rather than buoyant) forcing, but further investigation is needed to verify the

exact mechanisms for the sudden strengthening of the downdraft.

Although the simulated system is not nearly as large a long-lived squall line, some of the model results discussed above are consistent with previous idealized modeling results of squall lines and bow echoes. The strengthening cold pool and related mesohigh intensification behind the gust front played a key role in the transition process. As the gust front accelerated eastward, the convective updrafts along the central portion of the flanking line tilted westward (upshear) with height, creating a buoyantly forced horizontal pressure
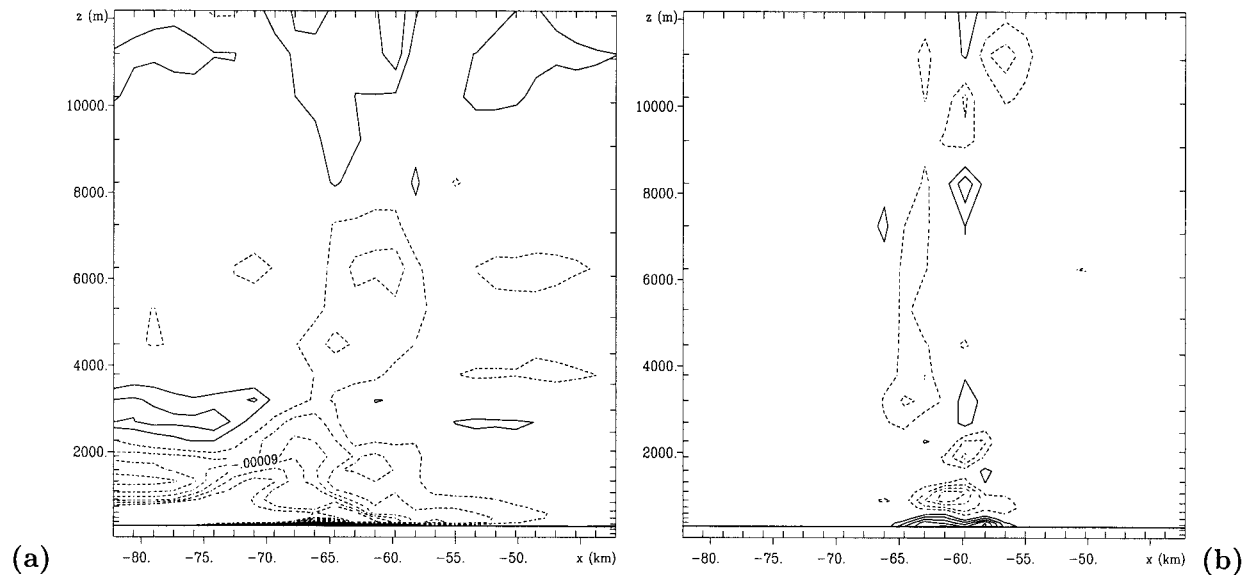
FIG. 21. Vertical cross sections of the along-line average of the forcing functions in the diagnostic perturbation pressure equation on grid 4 at 0037:30 UTC. Shown is (a) buoyancy forcing and (b) dynamic forcing. The contour interval for the forcing terms is 3×10^{-5} kg m^{-3} s^{-2}.

gradient at midlevels, which generated an elevated rear inflow extending 10–15 km behind the leading convective line. Although the rear inflow does not extend large distances behind the convective line in the HP supercell as it does in squall lines, it appears that the initial physical processes responsible for producing the strong winds in the two systems are the same. The current simulation differs somewhat from previous bow echo studies in that the shear forcing also became important in maintaining the horizontal pressure gradient at the back edge of the convective line as the transition progressed. This may help explain why bow echos associated with HP supercells are not long-lived. It has been hypothesized by Rotunno et al. (1988) that a "balance" between the horizontal vorticity generated at the outflow's leading edge and the ambient vorticity helps create deep lifting at the leading edge of the gust front, and helps maintain the longevity of the system. The strong acceleration into the back of the bow caused by both buoyancy and shear forcing may prevent this balance from occurring in this case.

Previous observational and modeling studies have also indicated that the development of "book-end" vortices plays a significant role in the development of bow echoes. Lee et al. (1992a,b) observed a single thunderstorm develop into a bow echo during the Joint Airport Weather Studies (JAWS) project. Their observed storm was different from the simulated storm in this study in that it developed in a weak shear environment, and was not rotating prior to bow echo development. Their results indicated that the bookend vortices that developed through tilting of ambient vorticity by a microburst were responsible for the development of the bow echo structure. Weisman (1993) also showed that the development

of bookend vortices in his simulated squall line bow echo enhanced the rear inflow and may have aided the development of a bow structure in the convective line. This idea will be investigated in the context of the current simulation in the next section.

c. Vorticity analysis

Previous modeling studies of supercells have demonstrated that classic supercells derive their midlevel rotation through tilting of ambient streamwise vorticity by the main updraft (Klemp and Wilhelmson 1978a,b; Klemp et al. 1981; Rotunno 1981; Weisman and Klemp 1982, 1984; Davies-Jones 1984). However, HP storms exhibit several characteristics generally not seen in classic supercells such as multicellular behavior (Foote and Frank 1983; Nelson 1987; Moller et al. 1988; Doswell et al. 1990; Moller et al. 1990, 1994). As was discussed in section 4, a time series of the vertical vorticity and condensate fields at many different vertical levels indicated that several small convective cells moved northward along the flanking line and then merged with the main mesocyclone at the northern end of the storm. The merger of "daughter cells" generated along the flanking line with the main storm updraft has been observed in some supercells (Lemon 1976; Barnes 1978a), although the role of these cells in supercell structure and morphology is unclear. Lemon (1976) proposed that these mergers could contribute to the longevity and severity of supercells. Kulie and Lin (1998) also found that the merger of cells from the flanking line into the main updraft played a vital role in maintaining the intensity and rotation in their simulation of an HP supercell. Here we will investigate this idea in the context of the present
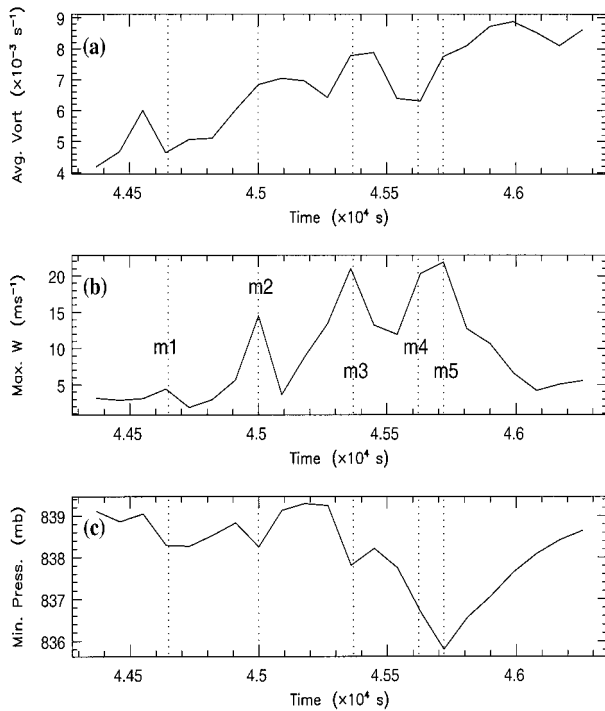
FIG. 22. A time series of (a) area average vertical vorticity at $z = 2$ km, (b) maximum vertical motion at $z = 2$ km, and (c) minimum pressure at $z = 1.3$ km in the low-level mesocyclone. Daughter cell merger events (m1–m5) are denoted with the dotted lines. The time series is from 0019:30 to 0051 UTC.

simulation. We also investigate the possibility that the flanking line may be a significant vorticity source for the mesocyclone in some HP supercells. This in turn may aid the storm's transition into a bow echo, and may help sustain the mesocyclone despite the fact that the mesocyclone is embedded in heavy precipitation.

A total of five daughter cell "merger" events could be identified in the simulation. Merger is defined as the time period that begins when a local vertical vorticity maximum (at $z = 3$ km) starts to lose its distinction as it approaches the mesocyclone, and ends when the local maximum is no longer distinguishable from the maximum associated with the mesocyclone. Following each merger, the mesocyclone intensified and increased in size. To investigate this issue, area averages and maximum and minimum values of pressure, vertical motion, and vertical vorticity were calculated in time over a 5.2 km × 5.2 km area around the center of the mesocyclone at each model level. This area was chosen since it is the approximate size of the early mesocyclone, assuring that vorticity increases in the analysis were due to increases in the magnitude of the vorticity and not because the mesocyclone increased in size. The immediate intensification of the mesocyclone during daughter cell merger events is particularly evident at low levels as shown in Fig. 22. Each merger event is characterized by a sudden increase in maximum vertical velocity, a drop in the minimum pressure, and usually leads to an

increase in the average vertical vorticity in the low-level mesocyclone. Note that although the area average vorticity decreases for a short time following merger, it remains higher than the values prior to merger, leading to a steady increase in low-level mesocyclone intensity between 0022 and 0047 UTC. In addition, the upper-level mesocyclone ($z = 8$ km) first became clearly visible around 0036 UTC (coinciding with the third merger event) indicating that the merger of daughter cells with the main mesocyclone may also increase the vertical extent of the mesocyclone.

The flow field surrounding the storm during its transition and the merger of the daughter cells from the flanking line with the mesocyclone suggests that the flanking line may be a vorticity source for the mesocyclone in this case. To investigate this possibility, a group of 20 particles was placed along the gust front where large vertical vorticity values existed at $z = 488$ m on grid 5 at 0030 UTC. Each of the particles represents an air parcel originating below cloud base along the band of upward motion at the leading edge of the gust front. Three-dimensional particle trajectories were then calculated for a 15-min period ending at 0045 UTC. Horizontal projections of the initial and final locations of the particles are shown in Fig. 23. All but the southernmost particles (in the initialization) ended up at various elevations in the mesocyclone at the northern edge of bow. The parcels took a wide range of trajectories before reaching their final locations in the mesocyclone, but the trajectories can generally be broken into four groups: 1) those transported into the upper troposphere in the convective updrafts along the flanking line but not transported into the mesocyclone region (particles 1, 2, 4); 2) those transported upward along the flanking line and advected into the midlevel mesocyclone (particles 3, 5, 7, 15, 16); 3) those that were carried upward for a time but eventually became part of the downdraft, ending up at low levels as part of the storm outflow (particles 11–14); and 4) those transported upward a short time while being advected into the low-level mesocyclone (particles 17–20).

Of the 20 particles released below cloud base along the gust front, 13 were advected into the mesocyclone. To explore the possibility that these air parcels could carry positive vertical vorticity into the mesocyclone, the vertical vorticity and vorticity tendencies were calculated along each parcel trajectory. The vertical vorticity calculated along four of these particle trajectories is shown in Fig. 24. Although the vertical vorticity along a given trajectory varied by as much as an order of magnitude, vorticity values remained positive throughout the analysis for 11 of the 13 particles advected into the mesocyclone. Thus, most parcels carried positive vertical vorticity into the mesocyclone region. The two exceptions were particles caught in a convective downdraft before entering the mesocyclone region near cloud base (approximately 1500 m). The vertical vorticity along these two trajectories changed from positive to
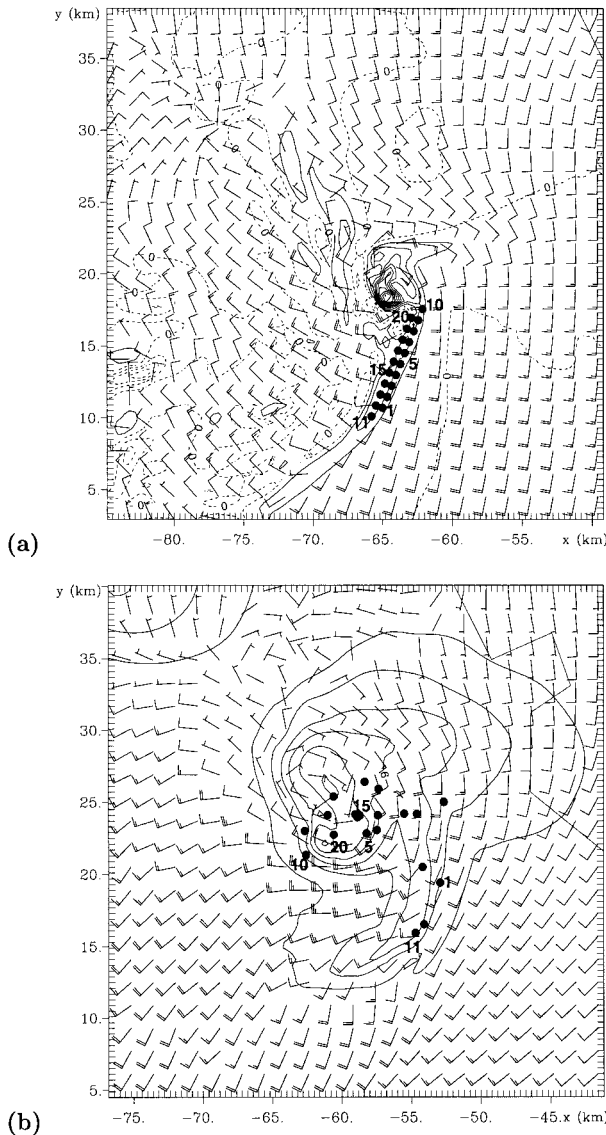
(a)

(b)

FIG. 23. Horizontal projections of the (a) initial and (b) final locations of the 20 particles released from the flanking line on grid 5. (a) Initial particle positions at $z = 488$ m overlayed on the vertical vorticity and horizontal wind fields. The particles were all initialized along the flanking line at 0030 UTC at $z = 488$ m as shown. Vertical vorticity is contoured every 5.0×10^{-3} s^{-1}. (b) Horizontal projection of the final particle positions overlayed with the total condensate and horizontal wind fields at $z = 2$ km at 0045 UTC. Condensate is contoured every 1.5 g kg^{-1}. Wind barbs are plotted at every fourth model grid point. The short (long) flag on the wind barb represents a wind speed of 5 m s^{-1} (10 m s^{-1}). A few of the particles have been labeled for reference.

negative as the parcels descended. Calculation of the vertical vorticity tendencies along the trajectories showed that tilting and convergence were responsible for maintaining the positive vertical vorticity along most of the trajectory paths as the particles were advected toward the mesocyclone.

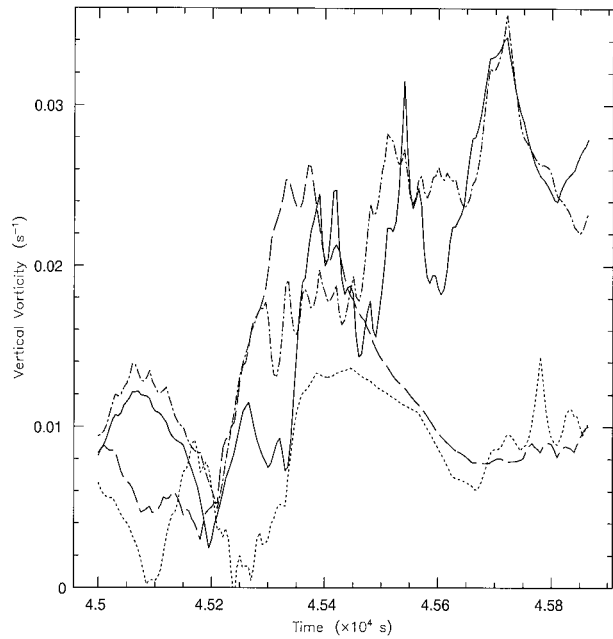The trajectory analysis above indicates that some of

FIG. 24. Time evolution of the vertical vorticity calculated along four parcel trajectories originating below cloud base along the gust front. Shown are vertical vorticity traces for particle 5 (solid), particle 9 (dashed), particle 16 (dot–dashed), and particle 20 (dotted).

the vertical vorticity in the mesocyclone is first generated along the flanking line and then advected northward into the mesocyclone. To more fully assess the importance of the flanking line as a mesocyclone vorticity source, a mesocyclone vertical vorticity budget was calculated at different vertical levels in the model. The model vertical vorticity equation in flux form (neglecting terms involving planetary vorticity and diffusion) is given by

$$\underbrace{\frac{\partial(\rho_0 \zeta)}{\partial t}}_{A} = \underbrace{-\frac{\partial(\rho_0 u \zeta)}{\partial x}}_{B} - \underbrace{\frac{\partial(\rho_0 v \zeta)}{\partial y}}_{C} - \underbrace{\frac{\partial(\rho_0 w \zeta)}{\partial z}}_{D}$$

$$- \underbrace{\zeta \frac{\partial(\rho_0 w)}{\partial z}}_{E} - \underbrace{\rho_0 \left[\frac{\partial w}{\partial x} \frac{\partial v}{\partial z} - \frac{\partial w}{\partial y} \frac{\partial u}{\partial z} \right]}_{F}, \quad (2)$$

where ζ is the relative vertical vorticity and ρ_0 is the base state density. Term A is rate of change of the vertical vorticity inside a specified volume in the mesocyclone, terms B, C, D are the vorticity flux divergence in the east–west, north–south, and vertical directions, respectively, term E is the stretching (or divergence) term and term F is the tilting term. Some care must be taken in interpreting some of these terms, however, since flows that tilt a vortex tube will also stretch it. To calculate the budget, each term in Eq. (2) was calculated on grid 5 in a volume 6.4 km $\times$ 6.4 km in the horizontal and 1 km in the vertical surrounding the center of the

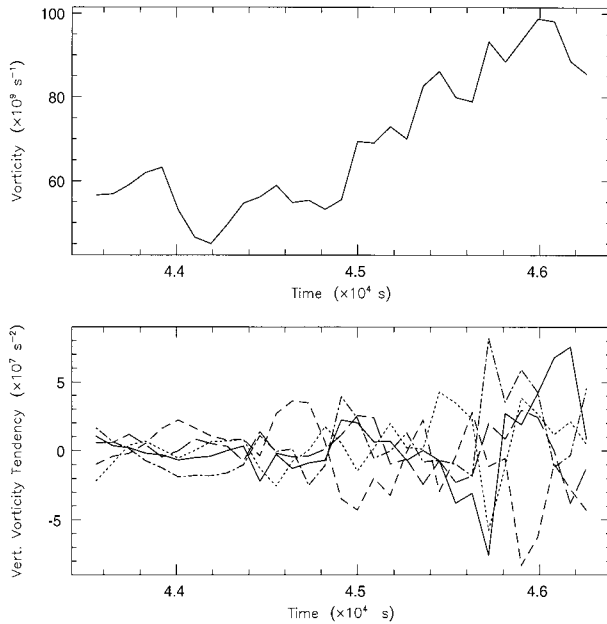FIG. 25. Time evolution of the (top) vertical vorticity and (bottom) vertical vorticity tendencies integrated over a 6.4 km × 6.4 km × 1 km volume centered on the mesocyclone at a height of 2 km. Lines plotted for the vertical vorticity tendencies are: east–west flux divergence (long dashed), north–south flux divergence (solid), vertical flux divergence (short dashed), tilting (dotted), and convergence (dot–dashed).

mesocyclone every 1.5 min from 0000 to 0100 UTC 1 July. This volume is somewhat arbitrary since the mesocyclone increased in diameter from ~5–6 km to ~15 km from 0030 to 0050 UTC during the analysis period. However, the vorticity budget calculated in both slightly smaller and larger volumes was qualitatively similar.

Results from the vorticity budget calculations at $z = 2$ km and at $z = 4.3$ km are shown in Figs. 25 and 26. In the low-level mesocyclone, the vertical vorticity flux into the mesocyclone was the dominant positive tendency throughout the early portion of the analysis (prior to 0027 UTC) as shown in Fig. 25. However, starting at 0022:30 UTC (44 550 s), the total horizontal flux of vorticity increased and became the largest positive vorticity tendency in the low-level mesocyclone between 0027 UTC (44 820 s) and 0033 UTC (45 180 s), with both east–west and north–south fluxes contributing equally. This period corresponds to the time just prior to and during the early portion of the storm's bow echo transition. A similar trend in the horizontal vorticity flux after 0030 UTC (45 000 s) was seen at all vertical levels in the storm below 6 km in the simulation, although at vertical levels above 2.5 km, the north–south flux of vorticity was dominant (see Fig. 26). At this time the cold pool intensified and the rear inflow began to develop, suggesting a connection between these morphological aspects and the intensification and growth of the mesocyclone. The north–south flux of vorticity was a significant positive vorticity tendency in the midlevel
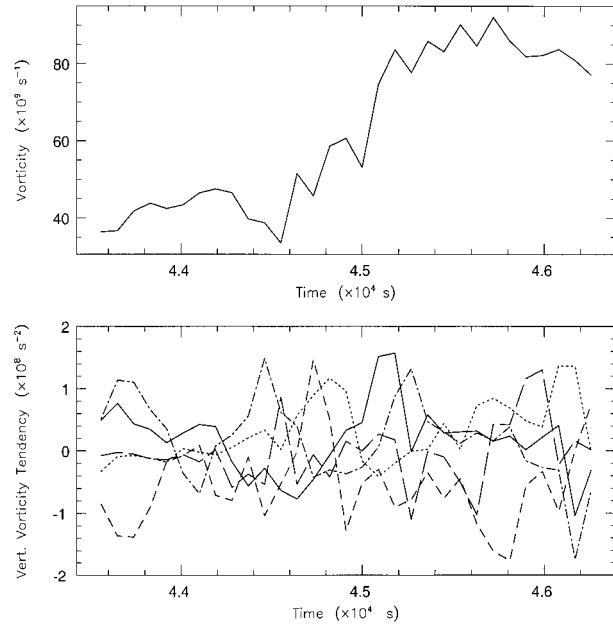
FIG. 26. As in Fig. 25 but at a height of 4.3 km.

mesocyclone through most of the bow echo transition from 0029 to 0041 UTC as shown in Fig. 26. Horizontal cross sections of the vorticity tendencies confirmed that this was due to northward vorticity advection along the southeast quadrant of the mesocyclone in the region of the flanking line (see Fig. 27). In the low-level mesocyclone, the vorticity tendencies due to the vertical vorticity flux and stretching became large from 0040:30 to
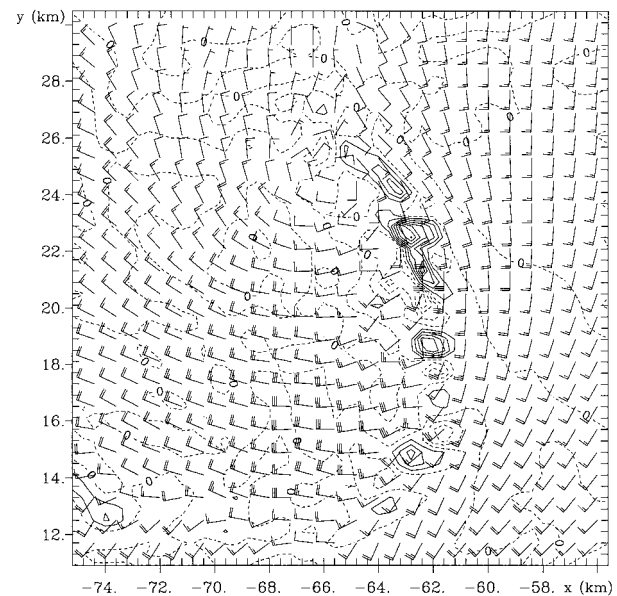
FIG. 27. Horizontal cross section of vertical vorticity advection by the v component of the wind at $z = 3$ km on grid 5 at 0034:30 UTC (contour interval 1.5×10^{-2} s^{-2}). Wind barbs are plotted at every other grid point. The long (short) flag on the wind barb indicates a speed of 10 m s^{-1} (5 m s^{-1}).

(a)

(b)

(c)

0043:30 (45 630 s–45 810 s) (Fig. 25). This trend could be seen at vertical levels in the storm below 3 km, and the time corresponds to the development of the second tornado in the simulation. The significance of this will be discussed in Part II.
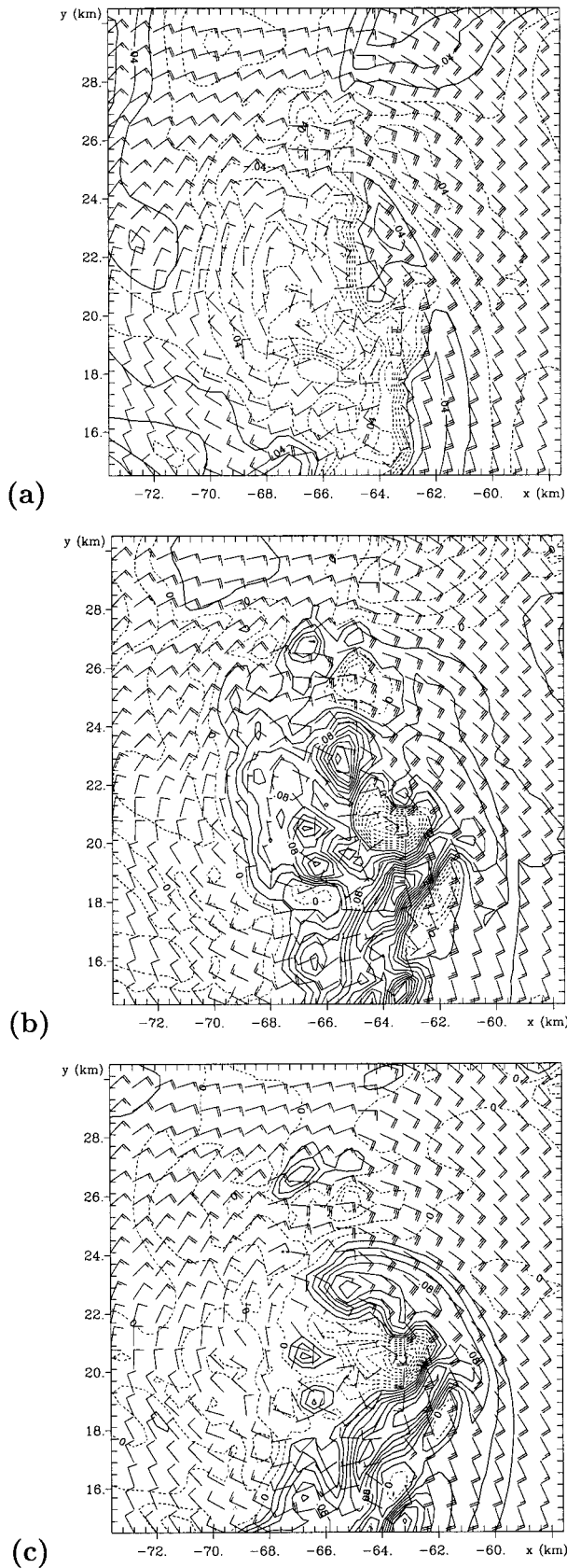
Tilting of the x component of vorticity into the vertical in the low-level mesocyclone became positive and increased significantly from 0036 UTC (45 360 s) to 0040 UTC (45 600 s) as can be seen in Fig. 25. This increase occurred at all vertical levels in the storm, but the tilting tendency only became significantly larger than the other tendencies at vertical levels between 2 and 4 km. An examination of horizontal cross sections of the vorticity tendencies revealed that the positive tilting was associated with increased vertical velocities in the mesocyclone, most notably in the low-level mesocyclone where both maximum positive and negative vertical velocities increased by a factor of 2 between 0030 and 0039 UTC. The positive tilting occurred in a band from the center of the mesocyclone to the southeast quadrant of the mesocyclone along the interface between the updraft and the downdraft. This region was west of the advancing gust front, which indicates that the horizontal vorticity being tilted did not originate in the storm environment but within the storm itself.

Since tilting becomes the largest positive vorticity tendency in the low-level mesocyclone during part of the bow-echo transition, it raises the question as to why this term suddenly becomes large at this time. As was discussed above, the increase in the tilting tendency is connected with the sudden increase in the updraft/downdraft strength in the mesocyclone. To investigate why the vertical velocities increased in the mesocyclone, the acceleration terms in the vertical momentum equation were calculated. The accelerations at 0033 UTC when the vertical velocities were rapidly increasing in the low-level mesocyclone are shown in Fig. 28. The buoyancy acceleration is generally negative throughout the mesocyclone region, the only exception being a small positive area along the east side where the flanking line intersects the mesocyclone circulation. This is not surprising since the mesocyclone was embedded in heavy precipitation at this time. The vertical pressure gradient acceleration shows an area of strong upward acceleration in the mesocyclone centered about $x = -66$ km, $y = 23$ km, and an area of strong downward acceleration centered near $x = -64$ km, $y = 21$ km. Returning to the perturbation pressure equation, this equation can also be written as

←

FIG. 28. Horizontal cross section of the (a) buoyancy, (b) vertical perturbation pressure gradient force, and (c) net vertical acceleration (contour interval 0.02 m s^{-2}) in the region surrounding the mesocyclone at $z = 3$ km at 0033 UTC. Wind barbs are plotted at every other grid point. The long (short) flag on the wind barb indicates a speed of 10 m s^{-1} (5 m s^{-1}).

$$-\nabla \cdot (c_p \rho_0 \theta_{ov} \nabla \pi) = \rho_0 [d_{ij} d_{ij}] - \frac{\rho_0}{2}[\omega_j \omega_j]$$

$$- \rho_0 \left[\frac{\partial^2 \ln(\rho_0)}{\partial z^2} w^2 \right] - \frac{\partial B}{\partial z}, \quad (3)$$

where d_{ij} is the three-dimensional rate of strain tensor, and ω_j is the three-dimensional vorticity vector. From Eq. (3), it can be seen that the pressure is lower where the magnitude of the vorticity is larger (Rotunno and Klemp 1982). It was shown in the vorticity tendency analysis that the vertical vorticity began to increase and the pressure decreased significantly at all levels in the mesocyclone just prior to and during the bow echo transition, which began at approximately 0030 UTC. Horizontal and vertical cross sections through the mesocyclone at 0034:30 UTC showed that the mesocyclone tilted toward the northwest with height below 4 km, while remaining nearly vertical above 4 km. This would create a rotationally induced downward-directed pressure gradient force on the southeast side of the low-level mesocyclone, and an upward-directed pressure gradient force along the northwest side, consistent with Fig. 28b. This suggests that a dynamically driven vertical pressure gradient force due to increased rotation in the mesocyclone was responsible for driving the upward motion and a significant fraction of the downward motion in the low-level mesocyclone during the transition. The net acceleration shows positive (negative) vertical acceleration on the north (south) side of the mesocyclone, creating a "split mesocyclone" structure as discussed by Lemon and Doswell (1979).

The average vertical vorticity at all levels in the mesocyclone doubled in the time period between 0030 and 0040 UTC (see Figs. 25, 26) with the largest increase occurring during and following the second daughter cell merger around 0030 UTC. Recall that this is the time at which the storm began its transition into a bow echo. Here we investigate the possibility that the strengthening of the mesocyclone and the development of the midlevel bookend vortices contributed to the storm's bow echo transition. Weisman (1993) performed idealized simulations of long-lived MCS bow echoes in which bookend vortices were produced. Using an idealized two-dimensional vortex model based on the strength of the bookend vortices in the MCS simulations, he estimated that between 30% and 50% of the rear inflow strength could be attributed to the bookend vortices during the mature phase of the system. Instead of using an idealized vortex model to estimate the rear inflow strength due to the midlevel vortices, the circulation was calculated around the vortices based on the area-average vorticity within a 10 km × 10 km box centered on each vortex. The average wind speed required to produce that circulation around the area was then calculated, assuming the wind speed is constant around a curve surrounding the area (as it would be in an idealized vortex). In the current simulation, the counterrotating vortices were

clearly visible over a 10-min period between 0035 and 0045 UTC. During this time period, the strength of the midlevel rear inflow was 35 m s⁻¹ between the vortices, with a local maximum between 40 and 45 m s⁻¹ along the southern flank of the cyclonic vortex (mesocyclone). Circulation calculations indicated that the average wind speed associated with the cyclonic vortex during this time period was 12 m s⁻¹, with an average wind speed of 3 m s⁻¹ around the anticyclonic vortex. Assuming linear superposition, this gives a rear inflow of 15 m s⁻¹ due to the counterrotating vortices. This estimate accounts for roughly 43% of the average rear inflow into the storm, in line with the estimates of Weisman (1993). Note from Fig. 22 that the circulation associated with the mesocyclone doubles between 0023 and 0035 UTC (44 500–45 300 s), which implies that the average wind speeds around the mesocyclone also double. Although the presence of the anticyclonic vortex aids in the strength of the rear inflow, its contribution is four times smaller than that from the cyclonic vortex. Thus in addition to the strong pressure gradient that develops behind the convective line, the intensification of the mesocyclone also appears to play a role in the storm's bow echo transition.

6. Summary and discussion

This study has documented the evolution of a simulated small convective cluster containing two supercells into a bow echo. The initial storm (S1) developed at the intersection between an old outflow boundary and a stationary front and maintained supercell characteristics during its entire lifetime. Other storms later developed to the west of S1, some of which also exhibited supercell characteristics during their lifetime. One of these storms (S2) merged with storms along the flanking line of S1, producing a larger convective storm in which S1 became the main mesocyclone, and S2 (losing its supercell characteristics) became part of a large flanking line.

While S1 had a classic supercell structure early in its life, it evolved into a large storm that had many characteristics of an HP supercell. The storm exhibited both multicell and supercell characteristics, which is often observed with HP supercells. In the simulation, there was heavy precipitation to the west-southwest of the mesocyclone, and the storm evolved into a rotating comma-head structure, which has been documented as one possible life cycle of HP supercells. The simulated storm also produced very heavy rain, strong winds, and weak tornadoes, all of which are common features of HP supercells. The propagation of smaller rotating cells located along the gust front into the main storm updraft has also been observed in other HP supercells (Lemon 1976), and has been observed in the field by the first author.

Although the available radar summaries for this case had insufficient time resolution to verify or refute the

model results, other observations of HP supercells indicate that they are frequently parts of larger convective clusters (Moller et al. 1990). Wolf (1998), Sabones et al. (1996), Goodman and Knupp (1993), and Bullas and Wallace (1988) documented cases where other convection (usually cells along a squall line) interacted with the southern periphery of a supercell, following which the supercell became HP in character and developed into a bow echo. In the simulation, there is also evidence that the interaction between convective cells triggered a series of events that led to the transition of the supercell into a bow echo. The environmental conditions ahead of the storm did not change significantly, precluding the possibility that a sudden change in the environmental conditions may have triggered the changes in the storm structure.

Shortly after the merger of S2 with the flanking line of S1, the precipitation rate increased significantly in the merger region, which led to increasing pressure behind the gust front causing the gust front to accelerate. As the gust front surged eastward, the convective updrafts along the central portion of the flanking line tilted westward (upshear) with height, creating a buoyantly forced horizontal pressure gradient at midlevels as was revealed in the diagnostic perturbation pressure analysis. This marked the storm's transition into a bow echo as an elevated rear inflow developed, extending 10–15 km behind the leading convective line. This evolution is similar to the idealized bow echo squall line simulations of Weisman (1993), but on a much smaller scale. However, later in the transition, shear forcing strengthened the horizontal pressure gradient, which further intensified the rear inflow.

The strengthening cold pool also had a significant impact on the evolution of the vorticity field and the mesocyclone in the simulation. As the gust front accelerated eastward in response to the strengthening cold pool, the vertical vorticity nearly doubled along the gust front due to increased tilting and convergence. This induced rotation on a larger scale, which altered the flow field south of the supercell, causing vorticity generated along flanking line to be advected into the mesocyclone. Trajectory calculations confirmed that air parcels originating at low levels along the flanking line carried positive vertical vorticity into the mesocyclone. Vorticity budget calculations in the mesocyclone also showed that vorticity advection from the flanking line into the mesocyclone was the largest positive vorticity tendency just prior to and during the early phase of the transition in both the low and midlevel mesocyclone, and remained a significant positive tendency in the midlevel mesocyclone throughout the bow echo transition. Thus, the flanking line is a source of vertical vorticity for the mesocyclone in this case, and may explain how the mesocyclone can be maintained in the HP supercell, even though it is completely embedded in heavy precipitation.

In simulated long-lived bow echo squall lines, the cyclonic vortex at the northern end of the line eventually becomes dominant. This has been attributed to the convergence of planetary vorticity enhancing the cyclonic vortex over a period of 6–10 h (Skamarock et al. 1994). In the present simulation, the cyclonic vortex at the northern end of the line also becomes dominant, but over a timescale of less than an hour, which is not long enough for the convergence of planetary vorticity to make a significant contribution. Results from this simulation suggest that vorticity generated along the flanking line and then advected northward into the mesocyclone may contribute to the dominance of the cyclonic vortex in this case.

Several vertical vorticity and condensate maxima developed along the flanking line and moved northward eventually merging into the mesocyclone during the lifetime of the HP supercell. A total of five "daughter cell mergers" were identified in the simulation, and with each merger, the low-level mesocyclone briefly intensified. This is consistent with studies by Lemon (1976) and Barnes (1978a), who showed that updraft velocity increased, surface pressure beneath the mesocyclone dropped, and the rotation in the mesocyclone increased following the merger of cells in the flanking line with the mesocyclone in several observed supercells. Kulie and Lin (1998) also speculated that mergers between smaller cells along the flanking line and the mesocyclone may have played an important role in maintaining storm-scale rotation and updraft intensity in their simulation of an HP supercell, but this idea was not fully explored. Although the individual merger events do intensify the low-level mesocyclone in the simulation presented here, the merger events are part of a larger process whereby advection of vorticity from the flanking line into the mesocyclone is acting to strengthen the mesocyclone through a significant depth of the troposphere.

Since the storm evolved into a bow echo structure in the hour following the addition of grids 5 and 6, the simulation begs the question: "is this the actual evolution of the system, or did the sudden addition of grid 5 cause the solution to deviate into the bow echo life cycle of an HP supercell?" To answer this question, the simulation was run from 0000 to 0100 UTC without grids 5–6 to see if the storm would evolve similarly in grid 4. The grid 4 results (not shown) looked like a "smoothed out" version of the grid 5 results (as expected, since grid 4 has coarser grid spacing and is not able to capture as many details as grid 5), indicating that the evolution of the storm into a bow echo was not a result of the addition of finer grids during the simulation.

Some recent idealized squall line simulations have linked the propagation of deep-tropospheric gravity waves upstream of the convective line to the development of the rear inflow jet behind the convective line (Pandya and Durran 1996; Schmidt and Cotton 1990). Even though the simulated storm in this study emits a

very large amplitude deep-tropospheric gravity wave just prior to the storm's transition into a bow echo, it was not clear that the gravity wave significantly contributed to the strong inflow behind the storm in this case. In the present simulation, the upstream propagating gravity wave did not propagate very far from the convective line before becoming a standing wave (with respect to the surface). The upstream wave also had a much smaller amplitude than the downstream propagating wave, and resembled the upward branch of the $m = 1$ mode discussed by Nicholls et al. (1991) and Mapes (1993). Perhaps environments that allow the propagation of the gravity waves upstream away from the storm marks the difference between environments that can support the larger MCC systems (in which deep-tropospheric convectively generated gravity waves can propagate large distances upstream of the convection) and environments that support isolated storms and smaller convective clusters (in which deep-tropospheric gravity waves cannot propagate upstream of the convection). However, this idea requires further investigation.

REFERENCES

Arakawa, A., and V. R. Lamb, 1981: A potential enstrophy and energy conserving scheme for the shallow water equations. *Mon. Wea. Rev.,* **109,** 18–36.

Avissar, R., and R. A. Pielke, 1989: A parameterization of heterogeneous land surfaces for atmospheric numerical models and its impact on regional meteorology. *Mon. Wea. Rev.,* **117,** 2113–2136.

Barnes, S. L., 1964: A technique for maximizing details in numerical weather map analysis. *J. Appl. Meteor.,* **3,** 396–409.

——, 1973: Mesoscale objective map analysis using weighted time-series observations. NOAA Tech. Memo. ERL NSSL-62, National Severe Storms Laboratory, Norman, OK, 38 pp.

——, 1978a: Oklahoma thunderstorms on 29–30 April, 1970. Part II: Radar–observed merger of twin hook echoes. *Mon. Wea. Rev.,* **106,** 685–696.

——, 1978b: Oklahoma thunderstorms on 29–30 April, 1970. Part III: Tornado characteristics inferred from damage tracks. *Mon. Wea. Rev.,* **106,** 697–703.

Bernardet, L. R., and W. R. Cotton, 1998: Multiscale evolution of a derecho-producing mesoscale convective system. *Mon. Wea. Rev.,* **126,** 2991–3015.

Bluestein, H. B., and C. R. Parks, 1983: A synoptic and photographic climatology of low-precipitation severe thunderstorms in the southern plains. *Mon. Wea. Rev.,* **111,** 2034–2046.

Brooks, H. E., and R. B. Wilhelmson, 1992: Numerical simulation of a low-precipitation supercell thunderstorm. *Meteor. Atmos. Phys.,* **49,** 3–17.

Browning, K. A., 1964: Airflow and precipitation trajectories within severe local storms which travel to the right of the winds. *J. Atmos. Sci.,* **21,** 634–639.

——, 1968: The organization of severe local storms. *Weather,* **23,** 429–434.

Bullas, J. M., and A. F. Wallace, 1988: The Edmonton tornado, July 31, 1987. Preprints, *15th Conf. on Severe Local Storms*, Baltimore, MD, Amer. Meteor. Soc., 438–443.

Calianese, E. J., Jr., A. R. Moller, and E. B. Curran, 1996: A WSR-88D analysis of a cool season, elevated high-precipitation supercell. Preprints, *18th Conf. on Severe Local Storms*, San Francisco, CA, Amer. Meteor. Soc., 96–100.

Clark, T. L., and R. D. Farley, 1984: Severe downslope windstorm calculations in two and three spacial dimensions using anelastic interactive grid nesting: A possible mechanism for gustiness. *J. Atmos. Sci.,* **41,** 329–350.

Davies, H. C., 1976: A lateral boundary formulation for multi-level prediction models. *Quart. J. Roy. Meteor. Soc.,* **102,** 405–418.

Davies-Jones, R. P., 1984: Streamwise vorticity: The origin of updraft rotation in supercell storms. *J. Atmos. Sci.,* **41,** 2991–3006.

——, and H. Brooks, 1993: Mesocyclogenesis from a theoretical perspective. *The Tornado: Its Structure, Dynamics, Prediction, and Hazards, Geophys. Monogr.,* No. 79, Amer. Geophys. Union, 105–114.

Doswell, C. A., III, 1985: The operational meteorology of convective weather. Vol. II: Storm–scale analysis. NOAA Tech. Memo. ERL ESG-15, 240 pp.

——, and D. W. Burgess, 1993: Tornadoes and tornadic storms: A review of conceptual models. *The Tornado: Its Structure, Dynamics, Prediction, and Hazards, Geophys. Monogr.,* No. 79, Amer. Geophys. Union, 161–172.

——, A. R. Moller, and R. Przybylinski, 1990: A unified set of conceptual models for variations on a supercell theme. Preprints, *16th Conf. on Severe Local Storms*, Kananaskis Park, AB, Canada, Amer. Meteor. Soc., 40–45.

Droegemeier, K. K., S. M. Lararus, and R. Davies-Jones, 1993: The influence of helicity on numerically simulated convective storms. *Mon. Wea. Rev.,* **121,** 2005–2029.

Finley, C. A., 1998: Numerical simulation of intense multi-scale vortices generated by supercell thunderstorms. Ph.D. dissertation, Atmos. Sci. Paper 640, Colorado State University, 297 pp.

Foote, G. B., and H. W. Frank, 1983: Case study of a hailstorm in Colorado. Part III: Airflow from triple-Doppler measurements. *J. Atmos. Sci.,* **40,** 686–707.

Fovell, R. G., and Y. Ogura, 1989: Effect of vertical wind shear on numerically simulated multicell storm structure. *J. Atmos. Sci.,* **46,** 3144–3176.

Goodman, S. J., and K. R. Knupp, 1993: Tornadogenesis via squall line and supercell interaction: The November 15, 1989, Huntsville, Alabama, tornado. *The Tornado: Its Structure, Dynamics, Prediction, and Hazards, Geophys. Monogr.,* No. 79, Amer. Geophys. Union, 257–264.

Grasso, L. D., 1996: Numerical simulation of the May 15 and April 26, 1991 tornadic thunderstorms. Ph.D. dissertation, Atmos. Sci. Paper 596, Colorado State University, 151 pp.

Hill, G. E., 1974: Factors controlling the size and spacing of cumulus clouds as revealed by numerical experiments. *J. Atmos. Sci.,* **31,** 646–673.

Houze, R. A., and C.-P. Cheng, 1977: Radar characteristics of tropical convection observed during GATE: Mean properties and trends over the summer season. *Mon. Wea. Rev.,* **105,** 964–980.

Imy, D. A., and K. J. Pence, 1993: An examination of a supercell in Mississippi using a tilt sequence. *The Tornado: Its Structure, Dynamics, Prediction, and Hazards, Geophys. Monogr.,* No. 79, Amer. Geophys. Union, 257–264.

Johns, R. H., and W. D. Hirt, 1987: Derechos: Widespread convectively induced windstorms. *Wea. Forecasting,* **2,** 32–49.

Klemp, J. B., and R. B. Wilhelmson, 1978a: The simulation of three-dimensional convective storm dynamics. *J. Atmos. Sci.,* **35,** 1070–1096.

——, and ——, 1978b: Simulations of right- and left-moving storms produced through storm splitting. *J. Atmos. Sci.,* **35,** 1097–1110.

——, and R. Rotunno, 1983: A study of the tornadic region within a supercell thunderstorm. *J. Atmos. Sci.,* **40,** 359–377.

——, R. B. Wilhelmson, and P. S. Ray, 1981: Observed and numer-

ically simulated structure of a mature supercell thunderstorm. *J. Atmos. Sci.,* **38,** 1558–1580.

Kulie, M. S., and Y.-L. Lin, 1998: The structure and evolution of a numerically simulated high-precipitation supercell thunderstorm. *Mon. Wea. Rev.,* **126,** 2090–2116.

Lafore, J.-P., and M. W. Moncrieff, 1989: Numerical investigation of the organization and interaction of the convective and stratiform regions of tropical squall lines. *J. Atmos. Sci.,* **46,** 521–544.

Lee, W.-C., R. M. Wakimoto, and R. E. Carbone, 1992a: The evolution and structure of a ''bow-echo–microburst'' event. Part I: The microburst. *Mon. Wea. Rev.,* **120,** 2188–2210.

——, ——, and ——, 1992b: The evolution and structure of a ''bow-echo–microburst'' event. Part II: The bow echo. *Mon. Wea. Rev.,* **120,** 2211–2225.

Lemon, L. R., 1976: The flanking line, a severe thunderstorm intensification source. *J. Atmos. Sci.,* **33,** 686–694.

——, and C. A. Doswell III, 1979: Severe thunderstorm evolution and mesocyclone structure as related to tornadogenesis. *Mon. Wea. Rev.,* **107,** 1184–1197.

LeMone, M. A., 1983: Momentum flux by a line of cumulonimbus. *J. Atmos. Sci.,* **40,** 1815–1834.

——, G. M. Barnes, and E. Zipser, 1984: Momentum flux by lines of cumulonimbus over the tropical oceans. *J. Atmos. Sci.,* **41,** 1914–1924.

Lilly, D. K., 1962: On the numerical simulation of buoyant convection. *Tellus,* **14,** 148–172.

Loveland, T. R., J. W. Merchant, D. O. Ohlen, and J. F. Brown, 1991: Development of a land-cover characteristics database for the conterminous U.S. *Photogramm. Eng. Remote Sens.,* **57,** 1453–1463.

Maher, Y., and R. A. Pielke, 1977: A numerical study of the airflow over irregular terrain. *Beitr. Phys. Atmos.,* **50,** 98–113.

Mapes, B. E., 1993: Gregarious tropical convection. *J. Atmos. Sci.,* **50,** 2026–2037.

Markowski, P. M., E. N. Rasmussen, J. M. Straka, and D. C. Dowell, 1998: Observations of low-level baroclinity generated by anvil shadows. *Mon. Wea. Rev.,* **126,** 2942–2958.

McPherson, R. A., and K. K. Droegemeier, 1991: Numerical predictability experiments of the 20 May 1977 Del City, OK supercell storm. Preprints, *Ninth Conf. on Numerical Weather Prediction*, Denver, CO, Amer. Meteor. Soc., 734–738.

Moller, A. R., and C. A. Doswell III, 1988: A proposed advanced storm spotter's training program. Preprints, *15th Conf. on Severe Local Storms*, Baltimore, MD, Amer. Meteor. Soc., 173–177.

——, ——, and R. Przybylinski, 1990: High-precipitation supercells: A conceptual model and documentation. Preprints, *16th Conf. on Severe Local Storms*, Kananaskis Park, AB, Canada, Amer. Meteor. Soc., 52–57.

——, ——, M. P. Foster, and G. R. Woodall, 1994: The operational recognition of supercell thunderstorm environments and storm structures. *Wea. Forecasting,* **9,** 327–347.

Nachamkin, J. E., and W. R. Cotton, 2000: Interaction between a developing mesoscale convective system and its environment. Part II: Numerical simulations. *Mon. Wea. Rev.,* **128,** 1225–1244.

Nelson, S. P., 1987: The hybrid multicellular–supercellular storm—An efficient hail producer. Part II: General characteristics and implications for hail growth. *J. Atmos. Sci.,* **44,** 2060–2073.

——, and N. C. Knight, 1987: The hybrid multicellular–supercellular storm—An efficient hail producer. Part I: An archetypal example. *J. Atmos. Sci.,* **44,** 2042–2050.

Nicholls, M. E., R. A. Pielke, and W. R. Cotton, 1991: Thermally forced gravity waves in an atmosphere at rest. *J. Atmos. Sci.,* **48,** 1869–1884.

Pandya, R. E., and D. R. Durran, 1996: The influence of convectively generated thermal forcing on the mesoscale circulation around squall lines. *J. Atmos. Sci.,* **53,** 2924–2951.

Pielke, R. A., and Coauthors, 1992: A comprehensive meteorological modeling system—RAMS. *Meteor. Atmos. Phys.,* **49,** 69–91.

Przybylinski, R. W., 1989: The Raleigh tornado—28 November, 1988:

A radar overview. Preprints, *12th Conf. on Weather Forecasting and Analysis*, Monterey, CA, Amer. Meteor. Soc., 186–191.

——, S. Runnels, P. Spoden, and S. Summy, 1990: The Allendale, Illinois tornado—January 7, 1989: One type of an HP supercell. Preprints, *16th Conf. on Severe Local Storms*, Kananaskis Park, AB, Canada, Amer. Meteor. Soc., 516–521.

——, J. T. Snow, E. M. Agee, and J. T. Curran, 1993: The use of volumetric radar data to identify supercells: A case study of June 2, 1990. *The Tornado: Its Structure, Dynamics, Prediction, and Hazards, Geophys. Monogr.*, No. 79, Amer. Geophys. Union, 241–250.

Rotunno, R., 1981: On the evolution of thunderstorm rotation. *Mon. Wea. Rev.,* **109,** 577–586.

——, and J. B. Klemp, 1982: The influence of the shear-induced pressure gradient on thunderstorm motion. *Mon. Wea. Rev.,* **110,** 136–151.

——, and ——, 1985: On the rotation and propagation of simulated supercell thunderstorms. *J. Atmos. Sci.,* **42,** 271–292.

——,——, and M. L. Weisman, 1988: A theory for strong, long-lived squall lines. *J. Atmos. Sci.,* **45,** 463–485.

Sabones, M. E., E. M. Agee, and M. Akridge, 1996: The Palaski County and West Lafayette, Indiana, tornadoes, 26–27 April, 1994: A case of supercell (mesocyclone) and squall-line bow echo interaction. Preprints, *18th Conf. on Severe Local Storms*, San Francisco, CA, Amer. Meteor. Soc., 746–750.

Schlesinger, R. E., 1980: A three-dimensional numerical model of an isolated thunderstorm. Part II: Dynamics of updraft splitting and mesovortex couplet evolution. *J. Atmos. Sci.,* **37,** 395–420.

Schmidt, J. M., 1991: Numerical and observational investigations of long-lived, MCS-induced, severe surface wind events: The derecho. Ph.D. dissertation, Colorado State University, 196 pp.

——, and W. R. Cotton, 1990: Interactions between upper and lower tropospheric gravity waves on squall line structure and maintenance. *J. Atmos. Sci.,* **47,** 1205–1222.

Simpson, J., and W. L. Woodley, 1971: Seeding cumulus in Florida: New 1970 results. *Science,* **172,** 117–126.

Skamarock, W. C., M. L. Weisman, and J. B. Klemp, 1994: Three-dimensional evolution of simulated long-lived squall lines. *J. Atmos. Sci.,* **51,** 2563–2584.

Smagorinsky, J., 1963: General circulation experiments with the primitive equations. I. The basic experiment. *Mon. Wea. Rev.,* **91,** 99–164.

Stensrud, D. J., and J. M. Fritsch, 1994a: Mesoscale convective systems in weakly forced large-scale environments. Part II: Generation of a mesoscale initial condition. *Mon. Wea. Rev.,* **122,** 2068–2083.

——, and ——, 1994b: Mesoscale convective systems in weakly forced large-scale environments. Part III: Numerical simulations and implications for operational forecasting. *Mon. Wea. Rev.,* **122,** 2084–2104.

Tao, W.-K., and J. Simpson, 1984: Cloud interactions and merging: Numerical simulations. *J. Atmos. Sci.,* **41,** 2901–2917.

Thorpe, A. J., and M. J. Miller, 1978: Numerical simulations showing the role of the downdraught in cumulonimbus motion and splitting. *Quart. J. Roy. Meteor. Soc.,* **104,** 873–893.

Tremback, C. J., and R. Kessler, 1985: A surface temperature and moisture parameterization for use in mesoscale numerical models. *Proc. Seventh Conf. on Numerical Weather Prediction*, Montreal, PQ, Canada, Amer. Meteor, Soc., 433–434.

Tripoli, G. J., and W. R. Cotton, 1980: A numerical investigation of several factors leading to the observed variable intensity of deep convection over south Florida. *J. Appl. Meteor.,* **19,** 1037–1063.

——, and ——, 1986: An intense, quasi-steady thunderstorm over mountainous terrain. Part IV: Three-dimensional numerical simulation. *J. Atmos. Sci.,* **43,** 894–912.

Vasiloff, S. V., E. A. Brandes, and R. P. Davies-Jones, 1986: An investigation of the transition from multicell to supercell storms. *J. Climate Appl. Meteor.,* **25,** 1022–1036.

Walko, R., W. R. Cotton, M. P. Meyers, and J. Y. Harrington 1995:

New RAMS cloud microphysics parameterization. Part I: The single moment scheme. *Atmos. Res.,* **43,** 29–62.

Weisman, M. L., 1992: The role of convectively generated rear-inflow jets in the evolution of long-lived mesoconvective systems. *J. Atmos. Sci.,* **49,** 1526–1847.

——, 1993: The genesis of severe, long-lived bow echoes. *J. Atmos. Sci.,* **50,** 645–670.

——, and J. B. Klemp, 1982: The dependence of numerically simulated convective storms on vertical wind shear and buoyancy. *Mon. Wea. Rev.,* **110,** 504–520.

——, and ——, 1984: The structure and classification of numerically simulated convective storms in directionally varying wind shears. *Mon. Wea. Rev.,* **112,** 2479–2498.

——, ——, and R. Rotunno, 1988: Structure and evolution of numerically simulated squall lines. *J. Atmos. Sci.,* **45,** 1990–2013.

Westcott, N., 1984: A historical perspective on cloud mergers. *Bull. Amer. Meteor. Soc.,* **65,** 219–226.

Wetzel, P. J., and J. T. Chang, 1988: Evapotranspiration from non-uniform surfaces: A first approach for short-term weather prediction. *Mon. Wea. Rev.,* **116,** 600–621.

Wicker, L. J., and R. B. Wilhelmson, 1995: Simulation and analysis of tornado development and decay within a three-dimensional supercell thunderstorm. *J. Atmos. Sci.,* **52,** 2675–2703.

Wilhelmson, R. B., and J. B. Klemp, 1978: A numerical study of storm splitting that leads to long-lived storms. *J. Atmos. Sci.,* **35,** 1974–1986.

——, and ——, 1981: A three-dimensional numerical simulation of splitting severe storms on 3 April, 1964. *J. Atmos. Sci.,* **38,** 1581–1600.

Wolf, P. L., 1998: WSR-88D radar depiction of supercell–bow echo interaction: Unexpected evolution of a large, tornadic, ''comma-shaped'' supercell over eastern Oklahoma. *Wea. Forecasting,* **13,** 492–504.